Uncovering Structure-Property Relationships with in-Situ Electrochemical Quantum Capacitance Spectroscopy

Mitchell Erlin Kaiser

A dissertation

submitted in partial fulfillment of the

requirements for the degree of

Doctor of Philosophy

University of Washington

2024

Reading Committee:

Jun Liu, Chair

Bo Zhang

Brandi Cossairt

Program Authorized to Offer Degree:

Chemistry

University of Washington

Abstract

Uncovering Structure-Property Relationships with in-Situ Electrochemical Quantum Capacitance

Mitchell Erlin Kaiser

Chair of the Supervisory Committee:

Jun Liu

Department of Materials Science and Engineering

Two-dimensional transition metal dichalcogenides (TMDs) have garnered significant attention due to their unique electronic properties and potential applications in various fields, including catalysis. Among these, monolayer molybdenum disulfide (MoS_2) has shown promise as a catalyst for the hydrogen evolution reaction (HER), which is crucial for sustainable hydrogen production. This thesis investigates the electrochemical performance and defect engineering of MoS_2 to enhance its catalytic efficiency. Chapter 1 provides a comprehensive introduction to two-dimensional materials with a focus on TMDs, emphasizing their electronic properties and potential as catalysts. It discusses the significance of hydrogen as a clean energy carrier and the

role of electrochemical water splitting in hydrogen production. The chapter also reviews the use of platinum-based and TMD catalysts in HER, highlighting the need for alternative, cost-effective materials. Chapter 2 focuses on the measurement and manipulation of the density of states (DOS) and defect states in two-dimensional materials using a novel electrochemical quantum capacitance spectroscopy (EQCS) technique. This method enables the detection of defect states and band edges under ambient conditions, offering significant advantages over traditional techniques that require cryogenic temperatures and ultra-high vacuum. The EQCS method is demonstrated on monolayer MoS_2, revealing the influence of mechanical strain on the electronic structure and catalytic activity toward HER. Results show that small mechanical strains can significantly enhance HER performance, providing insights into the relationship between strain, electronic structure, and catalytic efficiency. Chapter 3 delves into the characterization of defect evolution in monolayer MoS_2 during prolonged electrochemical cycling. Cyclic voltammetry and the EQCS measurement are used to illuminate the functional properties and electronic structure change over time. Conductive atomic force microscopy (cAFM) and X-ray photoelectron spectroscopy (XPS) capture the formation and aggregation of sulfur vacancies, which are identified as key active sites for HER. Initially, the introduction of sulfur vacancies enhances catalytic activity by lowering the hydrogen adsorption energy. However, as cycling continues, vacancy clusters form, leading to a decline in catalytic performance. The chapter provides a detailed analysis of the defect states and their impact on the electronic structure, supported by computational modeling. The findings of this thesis underscore the critical role of defect engineering in optimizing the electrochemical properties of two-dimensional TMDs for catalytic applications. The development of the EQCS technique represents a significant advancement in the in-situ characterization of electronic structures,

offering a powerful tool for future research. By elucidating the relationship between crystal structure, defects, electronic structure, and catalytic performance, this work paves the way for the rational design of high-performance functional materials.

Table of Contents

List of Figures

List of Tables

Acknowledgements

Completing this thesis would not have been possible without the contributions of many people. It truly takes a village to achieve something of this magnitude, and I am profoundly grateful for the interactions and relationships that have shaped me. I am an accumulation of the knowledge, skills, and kindness of others, and this work reflects the collective effort of everyone who has been part of my journey.

I would like to acknowledge the Department of Energy Office of Research Basic Energy Science project for funding my research during my PhD. The funding from this project has been crucial for the successful completion of my studies. I also thank the Clean Energy Institute for funding my fellowships and creating opportunities for training and personal development.

I would like to express my deepest gratitude to my principal investigator, Professor Jun Liu. During our very first meeting, he asked me to look out his office window onto the lake, people, cars, boats, airplanes, and mountains. He encouraged me to think about how our research could benefit society and the natural world. Taking a chance (that I hope he feels has paid off), he hired me on the spot, and accepted me into his lab in my second year of graduate school when I was in desperate need of a change. I am inspired by his humility and his desire to make a positive impact through science. He taught me to think like a scientist and to consider the broader context of our research.

Thank you to my mentors: Professor Matthew Yankowitz, who allowed me to use his facilities, provided insightful guidance, taught me condensed matter physics, and welcomed me as an honorary group member; Professor Mengyu Yan, who taught me the techniques that have been fundamental to my work, and how to interpret and collect data to tell a convincing scientific

story; Professor Jihui Yang, who engaged me in stimulating scientific debates and discussions, teaching me to question and think critically about claims in the literature; Doctor Maria Sushko, who, as the PI of my BES sub-project, provided theoretical calculations to explain my experimental results and guided me through the process of completing several projects; Professor Shuai Zhang, who helped me learn atomic force microscopy and acquire data using advanced techniques; Professor Hadi Zareie, who taught me the fundamental principles of atomic force microscopy, assisted with sample measurements, and imparted essential laboratory skills; and Doctor Danica Hendrickson, who, as my mentor during my CEI fellowship, helped me develop science communication skills, become a better educator, advocate for diversity, equity, and inclusion, and cheered me on throughout the challenges of my PhD.

I extend my heartfelt thanks to my thesis reading committee members, Professor Brandi Cossairt, Professor David Cobden, and Professor Bo Zhang, for their time, effort, and invaluable feedback that helped refine this thesis.

My colleagues and peers have been a tremendous source of support and camaraderie. I am particularly thankful to my lab mates Aaron Thomas, Anthony Romero, Bella Wu, Bhagyesh Trivedi, Cassidy Anderson, Doctor Sicen Yu, Minh Duong, Rose Lee, Varun Kumar, Wilson Ng, Ying Xia, Yuchun Guo, and Zhi Peng and Professor Jihui Yang's students Chris Tran, Doctor Yuzhou Zhou, Hao Tang, Julia White, Martin Brischetto, and Parker Steichen. They have created a welcoming and collaborative laboratory environment. I appreciate their help with experiments, the knowledge they've shared, and the levity they bring during challenging times.

To my adopted lab members in Professor Matthew Yankowitz's lab; Anna Okounkova, Dacen Waters, Derek Waleffe, Ellis Thompson, Florie Mesple, Manish Kumar, Toby Chu, and Xuetao Ma. Their willingness to include me as an honorary lab member, teach me specialized

techniques, share supplies and equipment, and answer my numerous questions about condensed matter physics, device fabrication, and scanning tunneling microscopy has been incredibly helpful.

Chaman Gupta and Yuhuan Meng have been excellent collaborators. Chaman Gupta helped with Raman and photoluminescence spectroscopy and taught me a great deal about optics. Yuhuan Meng assisted with photoluminescence spectroscopy and provided valuable insights into the theory of the optical properties of materials. I thank them both for their friendship.

I want to express my gratitude to the members of the MolES second floor lunch crew: Abdul Moeez, Jay Dua, Karen Li, Lorenzo Guio, Sankhya Hirani, and Wenhao Zhou. Their friendship, sharing of expertise, conversations ranging from intellectual to hilarious and absurd, and commiseration over the PhD experience have been irreplaceable.

Special thanks to the Molecular Engineering and Science and Nano Engineering and Science building managers, John Young and Allison Schroeder, for keeping the building and facilities in working order, lending tools, upgrading laboratory systems, ensuring safety, facilitating the delivery, movement, and installation of equipment, helping me find lost packages, and generally making MolES a pleasant place to work. I also appreciate Fam and the custodial team for keeping our workspace clean. They come in extremely early every day to ensure the building is ready and spotless. Their efforts have maintained our beautiful building and made it a productive and comfortable workspace. They do all of this with a cheerful attitude that brightens the day.

I am deeply indebted to my loving family - my parents, Doctor Diane Kaiser and Doctor John Kaiser, my brother, Jeffrey Kaiser, my sister-in-law, Kimberley Kaiser-Smith, and my beautiful nieces, Addicus and Juna Kaiser. Thank you for always being there to listen when I needed

someone to talk to during challenging times. You instilled in me a strong sense of ethics and morality, a robust work ethic, and a deep appreciation for education and knowledge. You gave me the confidence to pursue a PhD. My nieces, Addicus and Juna Kaiser, provided cuddles and reminded me of the importance of play, and to approach the world with a sense of wonder.

To my girlfriend of almost 6 years, Katherine Brunson; your unwavering love and support were everything during moments of doubt. Your encouragement kept me going when I felt like giving up. You gave me something to look forward to at the end of each day and reminded me to take breaks and appreciate life. You are incredibly caring and most certainly smarter than me, but I'm lucky you still like me anyway. You made our home a comfortable and peaceful haven and shared the burden of day-to-day tasks when I was overwhelmed. Thank you for your encouragement throughout this journey. I am so lucky to share a life with you.

Finally, Lavoisier, you bring immense joy to my life. You are a great listener, excellent company, and you have very soft fur. You truly live up to your namesake. Thank you for keeping my lap warm while I wrote this.

1 INTRODUCTION

1.1 Introduction to two-dimensional van der Waals materials and transition metal dichalcogenides

Two-dimensional (2D) materials are generally defined as materials having a regular elemental and special order with a thickness of a single to few atoms. Some of these materials exist as van der Waals (vdW) crystals; crystals composed of 2D material sheets with strong in-plane atomic bonding, but relatively weak out of plane interaction[1]. The unique layered structure enables these materials to be readily peeled apart into thinner layers by various exfoliation methods, even down to a single layer[2]. This was first demonstrated by K. S. Novoselov in 2004 when he isolated graphene, a single layer of graphite, by mechanical exfoliation with Scotch Magic Tape[3]. This discovery generated huge interest in discovering and understanding a whole host of two-dimensional materials[4].

An especially promising class of two-dimensional materials is transition metal dichalcogenides (TMDs). These are defined to have the formula MX_2, where M is a transition metal from groups IV through VI and X is a chalcogen, sometimes of two different identities. These exist in a sandwich structure, where the transition metal is positioned in between top and bottom layers of chalcogenides. TMDs exist in 1T (trigonal symmetry), 2H (hexagonal symmetry) and 3R (rhombohedral symmetry) phases. This, coupled to the many possible atomic combinations, results in permutations that are semi-conducting, metallic, and even super conducting[4].

The rich variety of intrinsic defects in these materials adds an additional knob to tune their properties. Examples are substitutional impurities, vacancies, grain boundaries, and adatoms. Intentional inclusion of these defects can be used to adjust the band and phase structures, enhance carrier transport, and create effective doping[5].

Additional benefits are gained in scaling down to two dimensions, especially in single layers. For instance, the bandgap of molybdenum disulfide (MoS_2) increases from a bulk value of 1.2 eV to 1.8 eV in the monolayer. A change from an indirect to direct bandgap is also facilitated. This yields advantages such as enhanced photo response, valley-selective optical excitation, moderate mobility, and gate-tunable conductivity[6]. 2D TMDs are also highly influenced by interfacial interaction, which can be exploited to obtain devices with designer functionalities. For instance, surface defects can be used to induce non-destructive doping with the desired carrier type and concentration. Carrier transport is also largely controlled by contact with electrodes and scattering from interfaces with a dielectric medium[7,8].

1.2 Catalytic applications of 2D TMDs

One application that can benefit from this surface-governed regime is heterogenous catalysis[9]. In TMD catalysts, as exemplified by MoS_2, enhanced catalytic activity is afforded by metallic edge sites, while the basal plane is relatively inert. These materials can be patterned to expose a high density of edge sites, resulting in markedly increased efficiency[10]. However, this method fails to take advantage of one of the biggest selling points for TMDs; their ability to be isolated as a single layer. As a monolayer, these materials have an extremely large surface area to volume and surface area to mass ratio. Activating the inert basal plane would result in cost and material efficient catalysts. This means introducing catalytically active sites and inducing an electronic structure that results in favorable catalytic performance.

Thus, to realize the full potential of these materials, methods to control charge carrier polarity, energy level, and concentration are necessary[11]. While standard methods such as ion implantation and substitutional doping are destructive to the desirable electronic properties of the materials due to disruption of the crystal structure, the high interfacial sensitivity of a monolayer presents an

opportunity for control of electronic properties by even relatively small concentrations of defects[12]. For applications like electrocatalysis of the hydrogen evolution reaction (HER), an important criterion for a good catalyst is that the free energy of the adsorbed species is close to that of the reactant and product[13]. This requires overlap of the density of states of the adsorbate and active sites on the catalyst[14]. In a 2D TMD catalyst, the energy of these states can be readily tuned via defect engineering, effectively modulating the adsorption energy at the active sites[15].

1.3 Hydrogen and clean energy

Modern civilization is heavily reliant on fossil fuels for energy, which accounts for nearly 80% of global energy consumption[16]. However, the combustion of these fuels releases significant amounts of CO_2 and other greenhouse gases, contributing to global warming and environmental degradation[17]. As the world's energy demand continues to grow, particularly in developing countries, the need for sustainable, clean energy sources becomes more critical. By 2050, global energy demand is expected to range between 600 and 1000 EJ, making the transition to renewable energy sources essential for mitigating climate change and reducing our carbon footprint[17].

Hydrogen is considered a promising alternative energy carrier due to its high energy yield of approximately 122 kJ/g, which is 2.75 times greater than that of hydrocarbon fuels[18]. When used in fuel cells, hydrogen produces only water vapor as a byproduct, making it an environmentally friendly option for electricity generation and transportation. The use of hydrogen in vehicles, either in combustion engines or fuel cells, can significantly reduce dependence on fossil fuels and decrease tailpipe emissions, contributing to cleaner air and reduced greenhouse gas emissions[19].

One of the most sustainable methods for producing hydrogen is water electrolysis, which involves splitting water into hydrogen and oxygen using electricity. This process can be powered by

renewable energy sources such as solar, wind, and geothermal energy, making it a carbon-neutral method of hydrogen production[20]. Hydrogen can effectively store energy from intermittent renewable sources like solar, wind, and geothermal energy. Solar energy can be harnessed to produce hydrogen through photovoltaic systems that convert sunlight into electricity, which then drives the electrolysis process[21]. Wind energy can also be stored as hydrogen through wind-to-hydrogen systems, which use excess electricity generated during high wind periods to produce hydrogen via electrolysis. This stored hydrogen can then be converted back to electricity when wind energy is insufficient, providing a reliable energy supply[22]. Geothermal energy offers another viable option, where high-temperature steam generated by geothermal sources can be used to drive electrolysis, contributing to continuous and stable hydrogen production. Similarly, a hydroelectric dam can also be applied to this application. This would be especially useful at night when power production hugely outpaces demand[23].

1.4 Electrocatalysis of the hydrogen evolution reaction

The hydrogen evolution reaction (HER) is of both fundamental and practical interest, particularly for applications in water splitting and fuel cells. An efficient hydrogen evolution electrocatalyst must possess several critical properties: high catalytic activity, stability under operational conditions, and cost-effectiveness[24]. The catalytic activity of an electrocatalyst is often depicted using volcano plots, which illustrate the relationship between catalytic activity and the hydrogen adsorption free energy[25]. For optimal performance, the adsorption of hydrogen should be balanced—neither too strong nor too weak—ensuring efficient hydrogen evolution with minimal energy losses[26].

Precious metals, particularly platinum (Pt), are widely recognized as the benchmark electrocatalysts for HER due to their exceptional catalytic properties. Platinum's near-ideal hydrogen binding energy facilitates rapid adsorption and desorption of hydrogen atoms, which is crucial for efficient hydrogen evolution. This balance allows hydrogen molecules to adsorb onto the catalyst surface, dissociate into atoms, and recombine to form hydrogen gas, which is subsequently released. This optimal binding energy results in minimal overpotentials, making Pt one of the most effective catalysts for HER[27]. Indeed, noble metal catalysts like Pt, Pd, and Ru exbibit ideal overpotentials for HER. Furthermore, Pt exhibits high stability and activity[24].

Despite their superior performance, the main drawback of using precious metal catalysts lies in their prohibitive cost and limited availability. Precious metals are expensive due to their scarcity and complex extraction processes, posing significant economic barriers to their widespread use in large-scale applications such as industrial water electrolysis[28]. The excessive cost of these materials impacts not only the initial setup of electrocatalytic systems but also their long-term sustainability and economic feasibility. Furthermore, the reliance on rare and expensive materials contradicts the goal of creating affordable and accessible clean energy technologies, essential for global energy transition efforts.

Given these challenges, significant research efforts have been directed towards developing alternative, non-precious metal electrocatalysts that can provide comparable catalytic performance at a lower cost. MoS_2 has garnered significant attention as a HER electrocatalyst due to its unique properties and electronic structure. It stands out for its catalytic activity, high earth abundance, cost-effectiveness, and structural adaptability[29].

Monolayer MoS_2 exists as a S-Mo-S sandwich structure, with approximately a 3 Å gap between layers, leading to an overall thickness of approximately 7 Å. Its in-plane lattice constant is

approximately 3.16 Å. As mentioned previously, monolayer MoS_2 has a high surface area, a property which is desirable in heterogenous catalysis[30].

Sulfur vacancies in MoS_2 act as active sites for HER, significantly enhancing its catalytic performance. These vacancies can be introduced through various methods, such as electrochemical reduction, H_2 or H_2O vapor etching, plasma treatments, and laser ablation. Studies have shown that the optimal concentration of sulfur vacancies can significantly improve HER performance by modulating the hydrogen adsorption energy, thereby enhancing catalytic activity. For instance, it was found that MoS_2 with sulfur vacancy concentrations between 12.5% and 15.62% exhibited the highest HER performance[31].

Strain engineering is another effective strategy to boost the catalytic performance of MoS_2. Applying tensile strain to MoS_2 can alter its electronic structure, optimizing the hydrogen adsorption free energy and enhancing catalytic activity[32]. The application of strain shifts the band edges of MoS_2, promoting more favorable hydrogen adsorption energies, lowering the overpotential required to tune the Fermi level into the conduction band, and improving HER kinetics[33].

Both defect and strain engineering are effectively methods to tune the electronic structure of monolayer MoS_2 to result in overlap of the MoS_2 density of states (DOS) with the hydrogen atom that is absorbed onto a catalytic site during the HER process[34]. Therefore, it is important to have a tool that can easily measure the DOS of electrocatalytic materials in ambient conditions so that the effect of efforts to modify the materials to enhance catalytic activity can be assessed both by the resulting functional properties, like catalytic performance, but also by understanding how various modifications alter the electronic structure. The development of such a tool, dubbed

"Electrochemical Quantum Capacitance Spectroscopy" is discussed in chapter 2, and it is applied to understand the mechanism behind the enhance of the HER activity of monolayer MoS_2 by the application of biaxial strain. In chapter 2, this tool is used to experimentally elucidate the effect of increasing sulfur vacancies on the electronic structure, and resulting functional HER catalytic properties, of monolayer MoS_2.

1.5 References

1 Xiong, Z., Zhong, L., Wang, H. & Li, X. Structural defects, mechanical behaviors, and properties of two-dimensional materials. *Materials* **14,** 1192 (2021).

2 Akinwande, D. *et al.* A review on mechanics and mechanical properties of 2D materials—graphene and beyond. *Extreme Mechanics Letters* **13,** 42–77 (2017).

3 Novoselov, K. S. *et al.* Electric field effect in atomically thin carbon films. *Science* **306,** 666–669 (2004).

4 Hu, Z. *et al.* Two-dimensional transition metal dichalcogenides: Interface and defect engineering. *Chemical Society Reviews* **47,** 3100–3128 (2018).

5 Susarla, S. *et al.* Quaternary 2d transition metal Dichalcogenides (TMDS) with tunable bandgap. *Advanced Materials* **29,** (2017).

6 Mak, K. F., He, K., Shan, J. & Heinz, T. F. Control of Valley polarization in monolayer MoS_2 by Optical Helicity. *Nature Nanotechnology* **7,** 494–498 (2012).

7 Allain, A., Kang, J., Banerjee, K. & Kis, A. Electrical contacts to two-dimensional semiconductors. *Nature Materials* **14,** 1195–1205 (2015).

8 Radisavljevic, B., Radenovic, A., Brivio, J., Giacometti, V. & Kis, A. Single-layer MoS_2 transistors. *Nature Nanotechnology* **6,** 147–150 (2011).

9 Tyagi, D. *et al.* Recent advances in two-dimensional-material-based sensing technology toward health and Environmental Monitoring Applications. *Nanoscale* **12,** 3535–3559 (2020).

10 Tsai, C., Chan, K., Nørskov, J. K. & Abild-Pedersen, F. Rational design of MoS_2 catalysts: Tuning the structure and activity via transition metal doping. *Catalysis Science & Technology* **5,** 246–253 (2015).

11 Bertolazzi, S., Gobbi, M., Zhao, Y., Backes, C. & Samorì, P. Molecular chemistry approaches for tuning the properties of two-dimensional transition metal dichalcogenides. *Chemical Society Reviews* **47,** 6845–6888 (2018).

12 Daukiya, L., Seibel, J. & De Feyter, S. Chemical modification of 2D materials using molecules and assemblies of molecules. *Advances in Physics: X* **4,** 1625723 (2019).

13 Hinnemann, B. *et al.* Biomimetic Hydrogen Evolution: MoS_2 nanoparticles as catalyst for hydrogen evolution. *Journal of the American Chemical Society* **127,** 5308–5309 (2005).

14 Chen, J. *et al.* Mechanism of highly enhanced hydrogen storage by two-dimensional 1T′ MoS_2. *Physical Chemistry Chemical Physics* **22,** 430–436 (2020).

15 Sun, Y. *et al.* First-principles study of the catalytic properties of co-doped molybdenum disulfide nanoribbons for the hydrogen evolution reaction. *Journal of Applied Physics* **128,** (2020).

16 Hosseini, S. E. & Wahid, M. A. Hydrogen production from renewable and Sustainable Energy Resources: Promising green energy carrier for clean development. *Renewable and Sustainable Energy Reviews* **57,** 850–866 (2016).

17 Bauen, A., Vuille, F., Berndes, G., Junginger, M. & Londo, M. Bioenergy. A sustainable and reliable energy source. A review of status and prospects. Executive Summary. https://inis.iaea.org/search/search.aspx?orig_q=RN:41031506 (2009).

18 Kapdan, I. K. & Kargi, F. Bio-hydrogen production from waste materials. *Enzyme and Microbial Technology* **38,** 569–582 (2006).

19 Chaubey, R., Sahu, S., James, O. O. & Maity, S. A review on development of industrial processes and emerging techniques for production of hydrogen from renewable and sustainable sources. *Renewable and Sustainable Energy Reviews* **23,** 443–462 (2013).

20 Barbaro, P. & Bianchini, C. *Catalysis for Sustainable Energy Production*. (Wiley-VCH, 2009).

21 Rodriguez, C. A., Modestino, M. A., Psaltis, D. & Moser, C. Design and cost considerations for practical solar-hydrogen generators. *Energy Environ. Sci.* **7,** 3828–3835 (2014).

22 Linneman, J. & Steinberger-Wilckens, R. Realistic costs of wind-hydrogen vehicle fuel production. *International Journal of Hydrogen Energy* **32,** 1492–1499 (2007).

23 Eftekhari, A. Electrocatalysts for hydrogen evolution reaction. *International Journal of Hydrogen Energy* **42**, 11053–11077 (2017).

24 Eftekhari, A. Electrocatalysts for hydrogen evolution reaction. *International Journal of Hydrogen Energy* **42,** 11053–11077 (2017).

25 Parsons, R. The rate of electrolytic hydrogen evolution and the heat of adsorption of hydrogen. *Transactions of the Faraday Society* **54,** 1053 (1958).

26 Miles, M. H. Evaluation of electrocatalysts for water electrolysis in Alkaline Solutions. *Journal of Electroanalytical Chemistry and Interfacial Electrochemistry* **60,** 89–96 (1975).

27 Tymoczko, J., Calle-Vallejo, F., Schuhmann, W. & Bandarenka, A. S. Making the hydrogen evolution reaction in polymer electrolyte membrane electrolysers even faster. *Nature Communications* **7,** (2016).

28 Xu, X. *et al.* Metallic molybdenum sulfide nanodots as platinum-alternative co-catalysts for photocatalytic hydrogen evolution. *Journal of Catalysis* **374,** 237–245 (2019).

29 Wang, Z. & Mi, B. Environmental applications of 2D molybdenum disulfide (MOS2) nanosheets. *Environmental Science & Technology* **51,** 8229–8244 (2017).

30 Li, X. & Zhu, H. Two-dimensional MoS_2: Properties, preparation, and applications. *Journal of Materiomics* **1,** 33–44 (2015).

31 Cao, Y. Roadmap and direction toward high-performance MoS_2 hydrogen evolution catalysts. *ACS Nano* **15,** 11014–11039 (2021).

32 Li, H. *et al.* Activating and optimizing MoS_2 basal planes for hydrogen evolution through the formation of strained sulphur vacancies. *Nature Materials* **15,** 48–53 (2015).

33 Datye, I. M. *et al.* Strain-enhanced mobility of Monolayer MoS_2. *Nano Letters* **22,** 8052–8059 (2022).

34 Ling, F. *et al.* Enhancing hydrogen evolution on the basal plane of transition metal dichalcogenide van der Waals heterostructures. *Npj Computational Materials* **5**, (2019).

2 MEASURING DENSITY OF STATES IN TWO-DIMENTIONAL MATERIALS WITH ELECTROCHEMICAL CAPACITANCE

Significant portions of this chapter are adapted from:

Mitchell Kaiser, Mengyu Yan, Maria L. Sushko, Yang Zhou, Ying Xia, Hao Tang, Chun-Chih Tseng, Matthew Yankowitz, Jihui Yang, Jun Liu. Measuring and Manipulating Density of States in Two-Dimensional Materials with Electrochemical Capacitance. Submitted to *Nature Materials*

Note for collaborative work: The design of the method of strain application and the fabrication of the cruciform devices was completed by Yang Zhou. Microdevice fabrication and electrochemical measurements were performed by Professor Mengyu Yan and Yang Zhou. The development of the EQCS technique was a joint effort between Professor Yan, yang Zhou, and myself. Computations were carried out by Doctor Maria Sushko. Portions of the interpretation of the electrochemical was guided by Professor Yan and Yang Zhou. Portions of the interpretation of the computational results were guided by Doctor Maria Sushko. AFM measurements and interpretation were performed by Ying Xia.

2.1 Abstract

Measuring and controlling the density of states (DOS) and defect states in two-dimensional van der Waals materials is crucial for comprehending their unique physical properties and enhancing their functional properties for practical applications. Typically, probing the electronic structure of materials necessitates cryogenic temperatures and/or ultra-high vacuum conditions, which limits the ability to observe the electronic structure of these materials under typical device operating conditions. Here, we introduce a novel in-situ electrochemical quantum capacitance spectroscopy

(EQCS) technique developed by our group for detecting the absolute energies of defect states and band edges in ambient conditions. This method is validated across various two-dimensional material systems and can be easily adapted to others. At room temperature, the highest energy resolution achieved is 116 meV, close to the theoretical limit of 91 meV (3.5kBT). The in-situ EQCS platform also enables real-time monitoring and manipulation of DOS in real-time, facilitating controlled enhancement of electrochemical reactions. Remarkably, band shifts induced by approximately 1% mechanical strain can amplify the catalytic activity for hydrogen generation by nearly an order of magnitude. The EQCS platform thus offers a powerful new approach for probing and manipulating the intrinsic DOS and defect states of 2D materials in ambient conditions.

2.2 Introduction

Defects in two-dimensional crystals endow these materials with unique properties that are not found in their pristine counterparts[1-3]. For instance, adjusting the defect states in two-dimensional (2D) MoS_2 can significantly boost its quantum yield from a mere 0.6% to over 95%, making it a highly promising candidate for next-generation light-emitting diodes[4]. Furthermore, tuning the defect states in MoS_2 can also improve its hydrogen evolution activity[5,6]. Effective defect engineering necessitates a comprehensive understanding of the defect states and the evolution of a material's electronic structure during various physicochemical processes. Modern experimental techniques for characterizing electronic structures are unable to monitor the evolution of electronic structures under realistic operating conditions. Usually, the density of states (DOS) and the associated defect states are characterized through methods such as scanning tunneling spectroscopy (STS)[7,8] and photoemission spectroscopy (PES)[9,10]. For example, STS investigations

have revealed that sulfur vacancies in monolayer (1-L) MoS2 introduce a peak in the bandgap of the DOS, signifying that these defects create in-gap states which enhance the catalytic activity of the material for the hydrogen evolution reaction (HER)[35]. Additionally, PES has provided experimental evidence for the indirect-to-direct bandgap transition that occurs at the 1-L limit of MoS_2[10]. While the effectiveness of these techniques is evident, employing STS and PES measurements to measure the electronic properties of 2D materials is difficult due to the stringent sample requirements of each technique. STS typically necessitates a clean, atomically flat substrate with sufficient conductivity, whereas PES requires highly uniform large single-crystalline domains. Moreover, both techniques demand either ultra-high vacuum or low temperatures to achieve high-quality data. The combined requirements for stringent sample fabrication, ultra-high vacuum conditions, and/or low temperatures make it challenging to characterize and understand these 2D semiconducting materials for practical applications.

2.3 Experimental

2.3.1 Device fabrication

The natural monolayer MoS_2 flakes were prepared via mechanical exfoliation from a bulk MoS_2 single crystal using scotch tape. Then, the MoS_2 nanosheet was transferred to a clean silicon wafer with a 285 nm oxide layer. The photoresist 495 PMMA A4 was spun on the silicon wafer at 800 rpm for 10 s and then 4000 rpm for 40 s. Afterward, the coated wafer was dried at 180 ^{o}C on a hot plate for 5 min. The same procedure was used to spin coat 950 PMMA A4. The electrodes were drawn by electron beam lithography (TESCAN VEGA scanning electron microscope with lithography package) on the silicon wafer with the two precoated PMMA layers. The PMMA layers are developed by using a pre-refrigerated 3:7 water/IPA aqueous developer. The typical developing time is 30 seconds but varies with the electron dose and beam intensity of the electron-beam

lithography procedure. A 5 nm Ti wetting layer and a 50 nm Au were deposited using an electron beam evaporator at a pressure of 5×10^{-6} Torr. The deposition rates for Ti and Au are ~0.2 and 0.8 nm/s, respectively. The PMMA layers and excess deposited metals are removed by soaking the device in acetone at 50ºC for 1 hour. An optical microscope is used to inspect the device and ensure only the Ti/Au electrodes and the target MoS_2 flake are left on the Si wafer. The soaking time of the nanodevice in acetone is extended if the extra Ti/Au is not totally removed in 1 hour. After lift-off, the sample is washed with isopropanol and dried with the N_2 three times. Afterward, a new layer of 950 PMMA A4 was spun on the silicon wafer as the resistive layer at 800 rpm for 10 s and then 4000 rpm for 40 s. The wafer was dried as before (at 180ºC on a hot plate for 5 mins). 495 PMMA A4 was then spun on the 950 PMMA A4 layer with the same spin and baking procedure. The well in the layered PMMA film was etched using electron-beam lithography and a 3:7 water/IPA aqueous developer to expose the interest area of the monolayer MoS_2 flake. Finally, a plastic electrolyte container (10 – 15 mL) was attached over the PMMA well to ensure a stable electrochemical environment during the electrochemical measurements.

The monolayer MoS_2 device on PET substrate is fabricated with a similar procedure to the one on silicon wafers with a 285 nm oxide layer. The monolayer MoS_2 was mechanically exfoliated on the PET substrate and searched under the optical microscope. One layer of PMMA A4 495 and two layers of PMMA A4 950 are spin-coated and dried on the PET substrate in turn. Then a 50nm layer of Cr was coated using a magnetron sputtering system for improving the conductivity in the coming electron beam lithography. Afterward, the electrodes are written with electron beam lithography. The coated Cr is removed with the chromium etchant and the PMMA is developed with a 3:7 water/IPA aqueous developer. A 5/50 nm Ti/Au electrode is further thermal evaporated

on the developed area. At the last, the whole device was stuck to designed biaxial beams for applying tensile strains.

For the device measured using Raman spectroscopy, the monolayer MoS_2 flakes were prepared by mechanical exfoliation onto clean silicon wafer with a 285 nm oxide layer. From here, the flake was placed onto a polyimide film coated as described previously with a 5/50 nm Ti/Au using the dry-transfer technique. This was done to ensure a flake large enough for the Raman measurement could be obtained. The film was coated with PMMA and then subjected to the EBL process to open a well using the procedure mentioned earlier. The film was then mounted on the center of a PET cross using a cyanoacrylate glue.

2.3.2 Measuring the capacitance and electrochemical window of ionic liquids

The capacitance and electrochemical window of ionic liquids were measured in a three-electrode electrochemical cell, in which the Pt-wire acts as the counter electrode, the glassy carbon electrode serves as the working electrode, and the Ag/AgCl/[BMIM][Cl] works as the reference electrode. Electrochemical impedance spectroscopy (EIS) is used to measure the ionic liquid capacitance within the frequency range of 10^6 to 0.1 Hz. Ten points were recorded per decade at a sinusoidal amplitude of 10 mV. The electrochemical window of ionic liquids is determined using cyclic voltammetry at a scan rate of 10 mV/s.

2.3.3 Electrochemical capacitance and tunneling spectrum

A graphite carbon counter electrode and an Ag/AgCl reference electrode were integrated into the previously fabricated nanodevice to form a three-electrode electrochemical system, in which the monolayer MoS_2 flake acts as the working electrode. For the Ag/AgCl reference electrode, 1-

Butyl-3-methylimidazolium chloride was dissolved in [BMIM][BF_4] with a final concentration of 0.1 M. This served the electrolyte in the reference electrode to stabilize the silver chloride concentration. During the electrochemical measurements, the ionic liquids, including [BMIM][BF4], [BMIM][PF6], and [EMIM][DCA] (Purchased from Sigma-Aldrich), were applied as the electrolyte. Electrochemical measurements were carried out by combining an electrochemical workstation (BioLogic SP-300) and a probe station. Staircase potentio electrochemical impedance spectroscopy (SPEIS) was used to measure the capacitance (C_{total}) at the MoS_2-electrolyte interface and the tunneling current (I) as a function of electrochemical potential. An electrochemical capacitance spectrum and electrochemical tunneling spectrum can be plotted using C_{total} *vs.* potential and I *vs.* potential, respectively.

In a typical experiment, we scanned the working electrode potential using SPEIS from its open circuit potential to -1.5 V *vs.* Ag/AgCl with a step potential of 5 mV. -1.0 V *vs.* Ag/AgCl corresponds to 3.23 eV *vs.* vacuum, which is ~0.5 eV higher than the MoS_2 conduction band minimum (CBM) as predicted by the calculation. Thus, the electrons fill the MoS_2 CBM during this procedure. For each potential step, a one-second waiting time is set to decrease the influence of electrochemical kinetics. The impedance is excited under a single sine mode at 5 Hz with a sinusoidal amplitude of 50 mV. Each capacitance was averaged with five measurements. When the working electrode potential approaches -1.5 V *vs.* Ag/AgCl, we directly scan back to 2.5 V vs. Ag/AgCl with the same frequency, amplitude, step potential, and step waiting time. During the scanning, C_{total} and I were recorded at each electrochemical potential.

The hydrogen evolution reaction polarization curve is measured with a 3-electrode electrochemical system, in which a saturated calomel electrode served as the reference electrode,

a graphite electrode as the counter electrode, the monolayer MoS_2 as the working electrode, and 0.5 M H_2SO_4 as the electrolyte. The polarization curve is cycled with a scan rate of 5 mV/s.

2.3.4 Confocal Raman spectroscopy

Raman spectra were acquired using a Renishaw inVia Confocal Raman Microscope equipped with a 532 nm laser and a 50x objective. The laser power was set to 1%, the grating to 1200 l/mm, and each spectrum was measured with four 10 second accumulations with an extended range from 200-600 cm^{-1}.

For the unstrained device, the PET cross with the monolayer MoS_2 flake was placed directly on the microscope stage. For the intermediate and large strain spectra, the same cross was mounted to the respective strain holder and the assembly was placed onto the microscope stage. For each measurement, the laser was centered in the middle of the well in the PMMA coating.

2.3.5 Atomic force microscopy (AFM)

The low magnification AFM image of the 2D MoS_2 device was captured in air with amplitude modulation mode on a Jupiter AFM (Asylum Research, CA) with RFESPA-75 probes from Bruker. The probes typically have a resonance frequency of 75 kHz and a spring constant of 3 N/m. The lattice-resolved AFM image of monolayer MoS_2 was captured in air with contact mode on a Jupiter AFM (Asylum Research, CA) with ARROW-UHFAuD probes from NanoWorld. The amplitude and deflection setpoint were controlled to maintain image quality without changing the surface topography. Offline data processing was done using Gwyddion SPM data analysis software.

Commercial AFM probes typically feature square pyramidal tips with a radius in the range of 2-10 nm. These probes are adept at resolving lattice structures on flat surfaces, such as the central areas of 2D MoS_2, where the probe is perpendicular to the sample surface[42]. However, in regions where the surface topology transitions sharply, like at the edges of 2D MoS_2 where perpendicular planes meet, the standard probe's inability to maintain an optimal angle with both planes hinders the resolution of edge features with accuracy, preventing the acquisition of an atomically resolved image of the MoS_2 edge under these experimental conditions.

2.3.6 Computational details

Single-layer MoS_2 with zigzag and armchair edges were modeled using 3D periodic model as 2D ribbons periodic in the direction along the edges and with at least 10 Å vacuum gap between the edges and a 15 Å vacuum gap between images of the basal planes was used to avoid interactions between periodic images. Point Mo- and S-defects were introduced either in the basal plane or on the edges. All atoms were fully relaxed during structural optimization.

Density functional theory (DFT) simulations of the electronic structure of MoS_2 ribbons were performed using periodic plane wave DFT implemented in VASP code [43, 44]. Generalized gradient approximation and projected augmented wave (PAW) potentials [45] were used with PBE exchange correlation functional [46] and the D2 Grimme dispersion correction [47]. Spin polarization was included in all calculations: 6 × 6 × 1 Gamma centred Monkhorst–Pack grid was used for k-point sampling of the Brillouin zone. Plane wave cutoff of 400 eV was used. The convergence criterion for geometric relaxation was set to 0.01 eV/ Å.

A periodic slab model was used for hydrogen chemisorption calculations. A single-layer MoS_2 slab with a S vacancy in the basal plane and hydrogen atoms decorating the vacancy was optimized

using the convergence criterion of 0.01 eV/ Å. The free energy of the adsorbed state was calculated as

$$\Delta G = \Delta E_{H^*} - \Delta E_{ZPE} - T\Delta S_{H,}$$

where ΔE_{H^*} is the hydrogen chemisorption energy, and ΔE_{ZPE} is the difference of the zero-point energy between the adsorbed state and the gas phase. Considering that the vibrational entropy of H* in the adsorbed state is very small, the entropy of 1/2 H_2 adsorption, $\Delta S_{H,}$ can be approximated as 1/2 of the entropy of H_2 in the gas phase at standard conditions. The hydrogen chemisorption energy was calculated as

$$\Delta E_{H^*} = E(MoS_2+nH) - E(MoS_2+(n-1)H) - 1/2\ E(H_2),$$

where $E(MoS_2+nH)$ is the total DFT energy for the MoS_2 layer with n hydrogen atoms adsorbed on the S vacancy, $E(MoS_2+(n-1)H)$ is the total DFT energy for (n-1) hydrogen atoms adsorbed on the V_S and $E(H_2)$ is the DFT energy for a hydrogen molecule in the gas phase.

2.4 Results and Discussion

2.4.1 Main

Here, we describe a new method for achieving near-theoretical resolution measurement of the DOS of 2D materials in ambient conditions that is free from the strict sample requirements necessitated for typical characterization of electronic structures. We dub this method "electrochemical quantum capacitance spectroscopy" (EQCS). The core principle is that the intrinsic electrochemical capacitance of a 2D material is directly proportional to its density of states. The quantum capacitance of 2D materials is measurable by electrochemical techniques if the electrolyte's double layer capacitance is extremely large compared to the quantum capacitance of the 2D material. The total capacitance (C_{total}) of an electrochemical cell consists of two components: the interfacial

capacitance of the counter electrode (C_{CE}) and the interfacial capacitance of the working electrode (C_{WE}). This relationship is quantified as the sum of two capacitors in series, and has the form $1/C_{total} = 1/C_{WE} + 1/C_{CE}$. When $C_{CE} \gg C_{WE}$, $C_{total} \approx C_{WE}$. Similarly, the electrochemical capacitance ($1/C_{WE}$) can actually be split into two contributions in series[11-13]. One of these is the double-layer capacitance of the interfacial electrolyte (C_{DL}), and the other is the capacitance of the solid electrode (C_E). For a semiconductor or 2D material electrode, the capacitance is proportional to its DOS, making C_E equivalent to C_Q, the quantum capacitance[14,15]. The total value of electrochemical capacitance can now be quantified according to the contributions of the double-layer and quantum capacitance as $1/C_{total} = 1/C_{DL} + 1/C_Q$, where $C_{total} \approx C_Q$ in the limit that $C_{DL} \gg C_Q$, making the measurable C_{total} proportional to the DOS of the 2D material. A key aspect of this method is identifying electrolytes with (i) a high double layer capacitance significantly larger than C_E and (ii) an electrochemical stability window wide enough to encompass the conduction band minimum (CBM) and valence band maximum (VBM) of 2D materials. This is illustrated in Figure 2.1e.

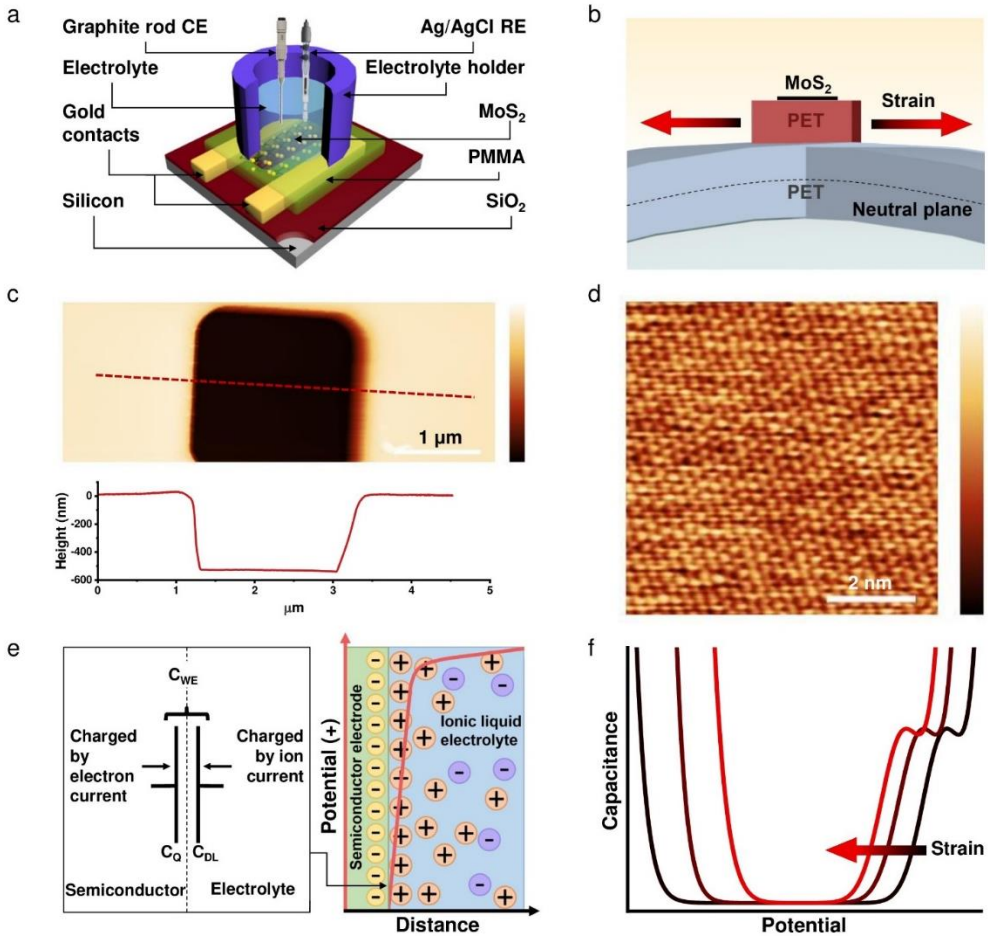

Figure 2.1 Experimental design and setup. **a.** Schematic of the device configuration used to measure the electrochemical quantum capacitance spectrum shown in Figure 2.2b. **b.** Schematic of the device configuration used in the strain-dependent measurements. The device is similar in construction to that in **a.** except that the silicon substrate is replaced with the flexible polymer polyethylene terephthalate (PET). Bending the device mounted on a PET cross (Figure 2.3a) causes the device to experience in-plane biaxial tensile strain. **c.** AFM image of the window in the PMMA layer used to expose the desired area of the 2D MoS_2 flake. The height profile corresponds to the red dashed line. Height range (gradient): 700 nm. **d.** High-resolution AFM image of the exposed monolayer MoS_2 in the 2D device. Height range (gradient): 70 pm. **e.** Diagram of the semiconductor electrolyte interface. This interface can be considered as a capacitor with a

capacitance value C_{WE}. The box on the left shows how this capacitance can be broken into two components, one being the quantum capacitance, C_Q, and the other being the electrochemical double layer capacitance, C_{DL}. The equations describing this system are shown above. **f.** Cartoons showing the effect of increasing biaxial strain on the electrochemical quantum capacitance, and therefore the density of states. The band gap decreases with increasing strain.

This study utilizes monolayer MoS_2 as the working electrode, with the ionic liquid 1-butyl-3-methylimidazolium tetrafluoroborate ([BMIM][BF4]) serving as the electrolyte. This ionic liquid meets the necessary criteria of high capacitance and a wide electrochemical window of approximately 3.5 V[16,17]. MoS_2 was selected as the electrode material due to its extensive applications in electronic systems and the availability of comprehensive experimental[18-20] and theoretical data[21] on its electronic structure, which can act as benchmarks for our electrochemical capacitance spectra. A schematic of the devices used for electrochemical measurements is depicted in Figure 2.1a. For strain measurements, the device construction is identical except for the substitution of the silicon substrate with PET (Figure 2.1b). PMMA is used to insulate the conductive components of the device from the electrolyte, with a window in the insulating layer isolating the electrochemical signal from the desired area of the monolayer MoS_2 flake. This window, with its clear boundaries, allows for the calculation of current density and areal capacitance (Figure 2.1c). An AFM image of the MoS_2 lattice within the PMMA window confirms that the pristine crystal structure is preserved throughout the device fabrication process (Figure 2.1d).

We employ the electrochemical technique staircase potentio electrochemical impedance spectroscopy (SPEIS) to measure C_{total} and the electrochemical tunneling current. Two scan frequencies, 5 and 100 Hz, are chosen to examine the DOS of the basal plane of MoS_2. At 5 Hz,

the capacitance of the interfacial [BMIM][BF4] layer is 61.7 μF/cm² (Figure 2.2a), significantly higher than the CBM value of C_Q (~4 μF/cm²) for monolayer MoS_2[22]. The positions of the VBM and CBM are distinctly captured in the EQCS measurement, showing a bandgap of 1.79 ± 0.147 eV (Figure 2.2b, Figure 2.S1). On top of the clear CBM position at 0.1 V vs. Ag/AgCl (4.83 eV vs. vacuum), another threshold appears around -0.3 V vs. Ag/AgCl. This feature aligns well with STS results at low temperatures[18,23,24] and the simulated shape of the conduction band of monolayer MoS_2 (Figure 2.2c). The electrochemical tunneling spectrum and dI/dV-V spectrum (Figure 2.S2) confirm the CBM and VBM positions of monolayer MoS_2 at 0.1 V and 1.9 V vs. Ag/AgCl, respectively. The simulated bandgap of 1.73 eV is approximately 9% smaller than the direct bandgap of 1.90 eV measured using optical spectroscopy[25]. The discrepancy is attributed to the systematic underestimation of the bandgap obtained using the the generalized gradient approximation with the PBE exchange-correlation functional[25,26]. When the frequency is increased from 5 to 100 Hz, C_{ion} drops dramatically to 0.8 μF/cm², and is smaller than C_E at the CBM of the monolayer MoS_2. Consequently, the quantum capacitance cannot be measured (black line in Figure 2.2b).

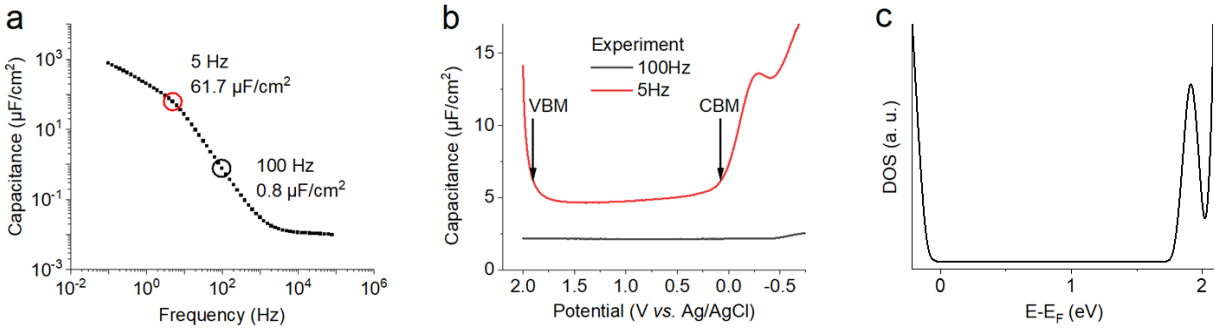

Figure 2.2. Electrolyte capacitances and MoS_2 electrochemical capacitance spectra at various frequencies. **a.** The frequency-dependent capacitance of BMIM-BF_4 at the open circuit potential. The capacitance of [BMIM][BF4] at 100 and 5 Hz is 0.8 and 61.7 μF/cm², respectively. **b.** The

electrochemical capacitance spectra of monolayer MoS_2 basal plane at 100 Hz (black line) and 5 Hz (red line). The measured bandgap of the monolayer MoS_2 basal plane is 1.8 eV. **c.** Calculated DOS of the single-layer MoS_2. Note that a/the PBE exchange correlation functional systematically underestimates the band gap of semiconductors [26,27]. E_F is the Fermi energy.

The EQCS measurement is next applied to characterize the electronic structure of the edges and defects of monolayer MoS_2. Both the zigzag edge and armchair edge of MoS_2 are studied separately. The edge types of MoS_2 are identified using second-harmonic generation spectroscopy (Figures 2.3a, b). Specifically, the zigzag and armchair directions of monolayer MoS_2 are known to correspond to the nodes and lobes of the SHG spectrum, respectively[28]. By comparing the and radius of our probes, which are further elucidated in the Supplementary Information section on AFM methodologies. However, our proposed edge structures are consistent with those imaged by STEM in other studies[32].

The estimate the energetic resolution of electrochemical quantum capacitance spectroscopy at room temperature was performed by calculating the full width at half maximum (FWHM) of the 25 peaks in the five EQCS spectra obtained in this study (Figure 2.S9). The highest energy resolution, indicated by the lowest FWHM, approaches 116 meV, which is close to the thermal Fermi function broadening at room temperature (3.5 kBT = 91 meV)[33].

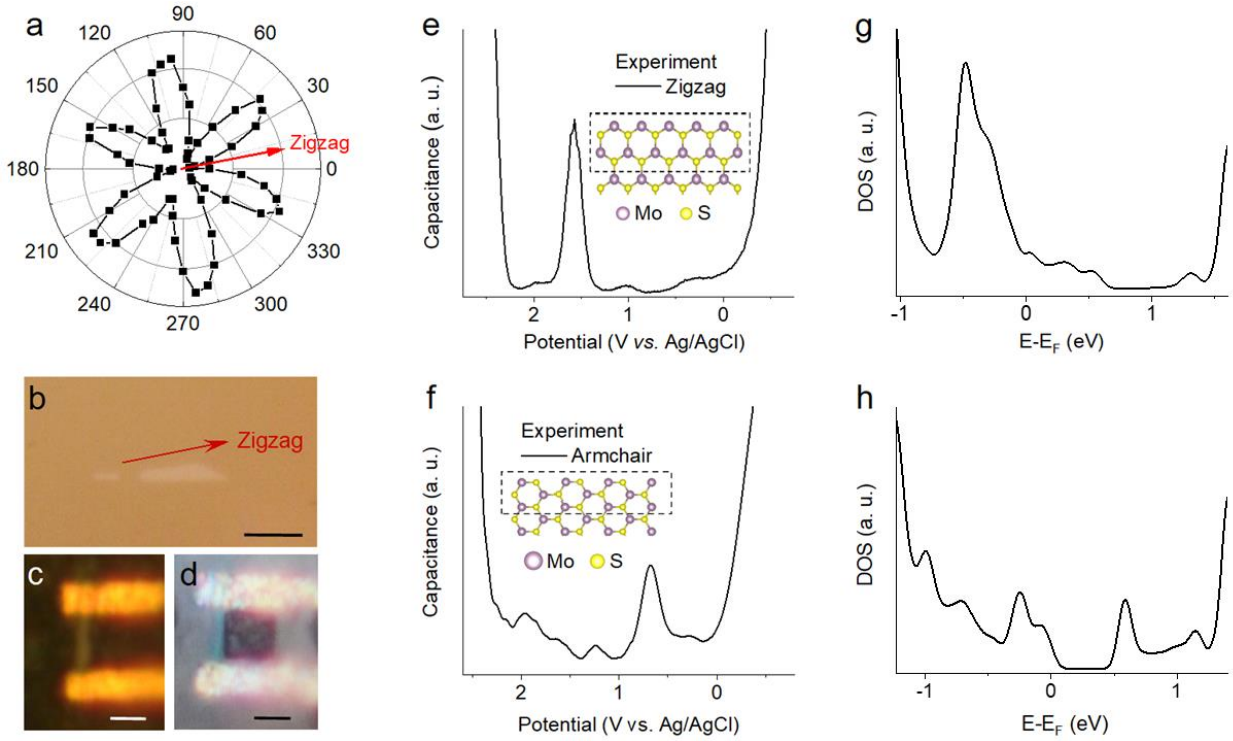

Figure 2.3. Edge-dependent defect energy levels in monolayer MoS_2. a. The resonant second-harmonic generation intensity parallel to the incident laser polarization as a function of the relative angle between the polarization direction of the laser and the crystal axis. **b.** A microscope image of the monolayer MoS_2. The zigzag (red arrow) edge of the monolayer sample is determined by the second-harmonic generation shown in Fig. 2a. **c, d.** Ti/Au electrodes are deposited on the MoS_2 (**c**). A PMMA950/PMMA495 bilayer is coated on the Ti/Au contacts and MoS_2, with a window (the dark brown area in Fig. 2d) opened to expose the zigzag edge (**d**). The scale bar is 5 μm. **e**. The electrochemical capacitance spectrum of the MoS_2 zigzag edge. The inset figure shows the proposed crystal structure at the zigzag edge, with the MoS_2-zigzag edge terminated by Mo atoms. **f.** The electrochemical capacitance spectrum of the MoS_2 armchair edge. The inset figure shows the proposed crystal structure at the armchair edge. **g, h**. Calculated density of states of the combination of the basal plane with zigzag (**g**) and armchair (**h**) edges. The edge and basal plane percentages are 0.04%/99.96% and 0.02%/99.98%, respectively.

The EQCS method not only identifies the defect states in 2D materials but also monitors the DOS around the conduction and valence band edges. This capability allowed us to explore how mechanical strain manipulates the conduction band of MoS_2 and the influence of band structure on electrochemical reactions. To investigate these effects, monolayer MoS_2 flakes were exfoliated onto a polyethylene terephthalate (PET) substrate and subsequently mounted on a PET plastic cross-shaped support. Biaxial tensile strain was applied to the PET substrate and monolayer MoS_2 flakes by bending the plastic cross support over dome-shaped glass (Figure 2.4a). The applied strain varies with changes in the glass curvature, and curvatures were selected to apply approximately 1% and 2% biaxial strain. The actual strain experienced by the monolayer MoS_2 flake was extracted from Raman spectra and plotted in Figure 2.4f. The intermediate strain value was found to be 0.6%, while the high strain value was 1.0%. The discrepancy between curvature-derived and measured strain likely arises from differences in Young's moduli between the armchair and zigzag directions of MoS_2, resulting in less efficient strain transfer between the substrate and MoS2 flake in the zigzag direction[41]. This smaller-than-expected strain makes the observed enhancement of the catalytic current even more significant. Electrocatalytic water-splitting (HER) was chosen as a model reaction, since it is extensively studied. Two unexpected results are observed in Figure 2.4b as a result of applying strain to the monolayer MoS_2 flake: (1) a distinct 3-zone polarization curve is measured, which is unusual for the HER in 0.5 M H_2SO_4, and (2) at -0.34 V vs. Ag/AgCl, the current density under 1% strain is five times higher than without strain.

EQCS was employed to uncover the correlation between the electronic structure and the shape of the polarization curves (Figure 2.4c). The electrochemical capacitance spectrum exhibits a plateau between -1.04 and -1.36 eV vs. Pt, just above the CBM of MoS_2. The width of the plateau is matches the 0.3 eV energy difference between the energy of the CBM at the **K** valley and the

energy of the **Q** valley[34]. The bandgap observed in the EQCS spectra clearly decreases from unstrained to 1% strained MoS_2. The downshift of the CBM shown is this spectra is partially responsible for the aforementioned increase in the catalytic current density. This is discussed in greater depth in section 2.4.2. Three regions are evident in the spectra, bound by points d1-d4.

A similar 3-zone electrocatalytic curve is observed in the unstrained monolayer MoS_2, indicating it is a common feature of the Tafel plots for 0%, 0.6%, and 1% strained monolayer MoS_2 (Figure 2.4e inset). Importantly, while the Tafel slope in Zone 1 decreases monotonically with an growing tensile strain, the Tafel slope in Zone 2 shows virtually no dependence on strain (Figure 2.4e). The decreasing Tafel slope in Zone 1 indicates the strained MoS_2 has a greater HER activity than the unstrained monolayer. This conclusion is supported by the changing shape of the polarization curves (Figure 2.4b) and the decreased bandgap exhibited by electrochemical capacitance spectra (Figure 2.4c) measured under strain. Further evidence is given by the fivefold increase in current density of 1% strained MoS_2 compared to the unstrained flake at -0.5 V vs. Ag/AgCl. This result aligns with recent observations of strain effects on the catalytic activity of MoS_2[35]. The experimental data demonstrates that if the HER kinetics are determined by a one-electron Volmer process, strain affects the electron transfer rate between MoS_2 and H^+. Using the Butler-Volmer method to fit the Tafel slopes for strained and unstrained MoS_2 shows a more than a fourfold increase in the electron transfer rate of monolayer MoS_2 under 1% strain compared to unstrained MoS_2[35].

2.4.2 Theoretical discussion

While the observed phenomena are complex, a preliminary discussion of the results and a proposed mechanism are made possible by comparison to simulation. As shown by the simulated CBM band in Figure 2.4d, there are 4 steps for the electrons to fill the **K**- and **Q**-valleys, which results in a 3-zone polarization curve during electrocatalysis. In the electrochemical environment, during **Step 1**: the Fermi level, tuned by the applied potential η, moves from open circuit potential up to the CBM at the **K**-point, where electrons are injected into the **K** valley. Thus, the DOS starts to increase at ~0.8 V (Figures 2.4c and 2.4d1. Here, the electrons in the **K** valley can transfer to H^+ at the MoS_2-electrolyte interface to form absorbed H atoms that can combine to form H_2. Hence, an onset potential close to -0.197 V *vs.* Ag/AgCl is observed in the 1% strained monolayer MoS_2. Because the electrochemical experiments are performed at room temperature, there is a ~3.5 k_bT thermal broadening of the Fermi function[33]. The tuning of the Fermi level (with thermal broadening represented as blue rectangles) position by applied potential is shown in Figure 2.4d1 – d4. **Step 2**: the Fermi level moves from the bottom of **K** valley up to the bottom of **Q** valley (Figure 2.4d2). There is no significant increase in the DOS, since the curvature of the band is zero and no additional states are available at other points in the band structure in this energy range (Figure 2.S7). Hence, a plateau appears between the d2 and d3 points in Figures 2.4b and 2.4c. **Step 3**: the Fermi level enters the **Q** valley (Figure 2.4d3). In this step, electrons in both the **K** and **Q** valleys contribute to the DOS, resulting in a rapid increase in the quantum capacitance and current density visible in the EQCS spectrum and HER polarization curve, respectively. **Step 4**: the Fermi level continues to shift upwards in energy (Figure 2.4d4). States between the **K** and **M** points become available (Figure 2.S7), resulting in further enhancement of both the DOS and catalytic current.

The mechanism for the enhanced HER activity and appearance of a more distinctive 3-zone electrocatalytic curve with increasing strain becomes apparent when considering the evolution of the band structure around the K- and Q-points. This is explored in Figure 2.4e, which shows the calculated band diagrams under 0, 1, and 2% strain. At 0% strain, the bandgap is direct and has a value of 1.74 eV, close to the value obtained from the quantum capacitance spectrum (Figure 2.2b). However, when 1% strain is applied, three changes occur: (i) The bandgap decreases to 1.24 eV; (ii) the bandgap undergoes a direct-to-indirect transition as the valence band maximum moves to the Γ-point; (iii) the K- and Q-valleys move downward and closer together in energy. The overall decrease in energy of the conduction band results in a higher catalytic current at low applied potential (η) and exaggerates the appearance of the 3-zone electrocatalytic curve, while the downshift of the Q-valley to the conduction band edge enhances the catalytic current at lower applied potential. With 2% strain, the bandgap further decreases to 1.1 eV. Again, the conduction band drops in energy, though not as far as is seen between 0 and 1% strain. This explains the smaller enhancement of the current between points d1 and d2 in Figure 2.4b and the smaller decrease of the Tafel slope between 0.6 and 1% strain (Figure 2.4g). Finally, the region in the electrocatalytic curve between points d2 and d3 flattens as the Q-valley shifts up in energy away from the K-valley.

Interpreting the strain dependence of the electron transfer rate requires considering several physicochemical processes at electrode/catalyst/electrolyte interfaces. These include the rate of electron hopping conductivity between the gold electrode and MoS_2, the rate of local electron transfer to adsorbed H^+ at active sites (mainly S-vacancies on MoS_2 basal plane and edges), the rate of H^+ adsorption, H diffusivity, and H_2 desorption at active sites. Given the complexity of the processes involved, identifying a single descriptor of the catalytic activity of MoS_2 towards HER

is desirable. It has been proposed that hydrogen reaction free energy may be such a descriptor to facilitate the computational screening of various catalysts[36,37]. The ideal value of reaction free energy is zero, corresponding to a thermoneutral state of the adsorbed atomic hydrogen and efficient electron/proton transfer followed by hydrogen release[36]. The calculated strain dependence of hydrogen reaction free energy supports the experimental observation that strained MoS_2 demonstrates higher catalytic activity (Figure 2.4f). Specifically, simulations predict a monotonic decrease in the absolute value of the hydrogen reaction free energy with an increase in strain. The effect can be rationalized as a combination of strain-induced changes in the band structure of the pristine MoS_2 layer and local changes in the surface relaxation, electronic structure, and electrostatic potential at V_S sites. The changes in the band structure led to the decrease of the MoS_2 bandgap with an increase in strain. The bandgap decreases because the lowest energy states in the K-valley down-shift with respect to the Fermi level in the absence of an applied potential[38]. Strain does not affect the relative position of states in the Q-valley with respect to the Fermi level [38], which might explain the independence of the Tafel slope with respect to strain in Zone 2. Although the electron density at the Fermi level is largely delocalized over the MoS_2 surface, the presence of S vacancies induces fluctuations in the electron distribution. The local effects of strain reveal themselves in the enhancement of fluctuations in electron density at the vacancy site, which leads to stronger hydrogen polarization and higher chemisorption energy. The hydrogen chemisorption energy changes from -0.09 eV to -0.15 eV, and finally -0.17 eV with an increase in strain from 0% to 1% to 2%, respectively.

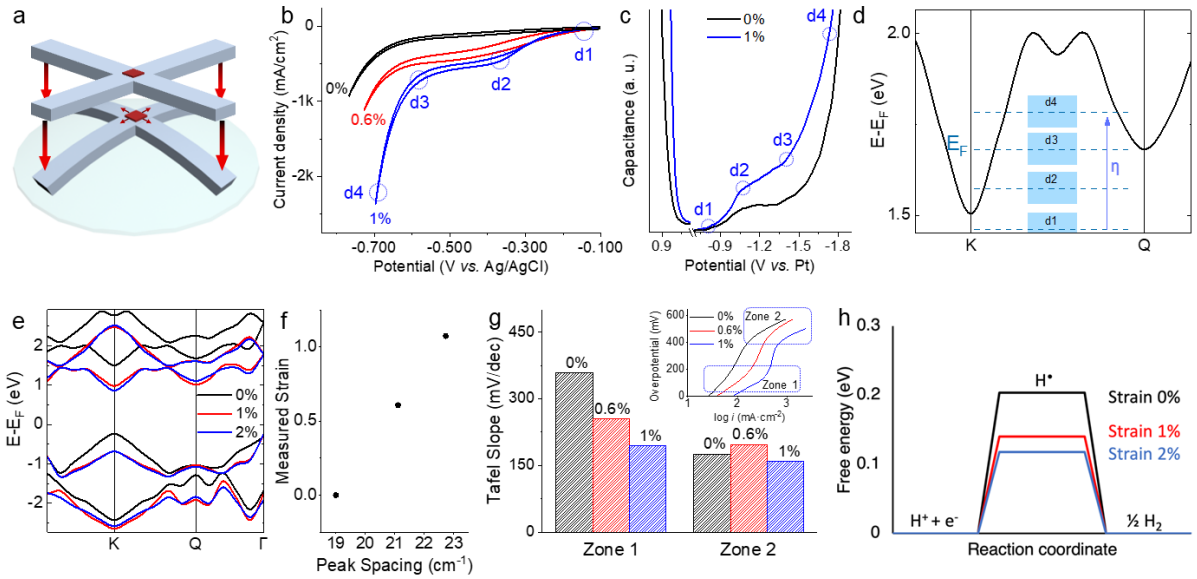

Figure 2.4. Strain modulated band structure and enhanced hydrogen evolution reaction. a. Schematic figure of the device setup for applying biaxial strain. Bending the PET cross over a curved platform results in biaxial tensile strain on the monolayer MoS_2, demonstrated by the black and red arrows. The tensile strain is increased when the bending radius decreases. **b.** The polarization curves of 0%, 0.6%, and 1% strained monolayer MoS_2 in 0.5 M H_2SO_4 at a scan rate of 5 mV/s. **c.** The electrochemical capacitance spectrum of monolayer MoS_2 at 0% and 1% strain. **d.** Calculated conduction band minimum showing the 4 steps for electrons to fill the **K**- and **Q**-valleys, resulting in a 3-zone polarization curve in the electrocatalysis. The Fermi level is tuned by the applied electrochemical potential η. Fermi broadening at room temperature is shown by the light blue rectangles. **e.** Calculated band diagrams of 0% (black lines), 1% (red lines), and 2% (blue lines) strained monolayer MoS_2 centered around the **K**- and **Q**- points. The Fermi level is shifted to 0 eV. See Figure 2.S7 for more detail. **f.** The measured strain extracted from the interpeak spacing of the A_{1g} and E^1_{2g} Raman modes. The calibration factors used are 1.02 cm^{-1}/% and 4.48 cm^{-1}/% for the A_{1g} and E^1_{2g} modes, respectively[35]. See SI for details on the calculation. **g.** The

Tafel slope values of two potential ranges of 0%, 0.6%, and 1% strained monolayer MoS_2. The inset is the Tafel slope of 0%, 0.6%, and 1% strained monolayer MoS_2. **h**. The calculated free energy diagram for hydrogen evolution at a potential $U = 0$ relative to the standard hydrogen electrode on the surface of unstrained and strained MoS_2.

2.4.3 Electrolyte selection

The measurements of the DOS of MoS_2 were made possible through the choice of an electrolyte that has two distinct features. The electrolyte needs high capacitance and a stability window that spans beyond the valence and conduction band edges of the material. In addition to [BMIM][BF4], which was used in the above experiments, we investigated two other commercially available ionic liquids, 1-Ethyl-3-methyl-imidazolium-dicyanamide ([EMIM][DCA]) and 1-butyl-3-methylimidazolium hexafluorophosphate ([BMIM][PF6]). Of the three electrolytes, [EMIM][DCA] exhibited the highest C_{ion}, exceeding 120 μF/cm² at 5 Hz (Figure 2.5a), although it has a smaller electrochemical stability window than [BMIM][BF4] or [BMIM][PF6] (Figure 2.5b). Unfortunately, [BMIM][PF6] also exhibits the lowest capacitance. To assess the alignment of electrochemical stability windows of these ionic liquids with the band edges of various 2D materials[39,40], their measured electrochemical stability windows were converted into absolute energies (eV vs. vacuum) (Figure 2.5c). As seen in figure 2.5c, [BMIM][BF4] is suitable for measuring the DOS and defect states of all of the 2D semiconductors depicted in Figure 2.5c. On the other hand, [EMIM][DCA] is best suited to measure DOS of 2D materials with high C_E and a narrow bandgap. While [BMIM][PF6] exhibits the largest stability window, its capacitance is too small to be used in this measurement. To demonstrate that the EQCS method is extendable to other material systems, we employed this technique to measure the DOS of bulk black phosphorus

(Figure 2.S11). Notably, the bandgap extracted from the black phosphorus device matches the literature value of approximately 0.3 eV[41].

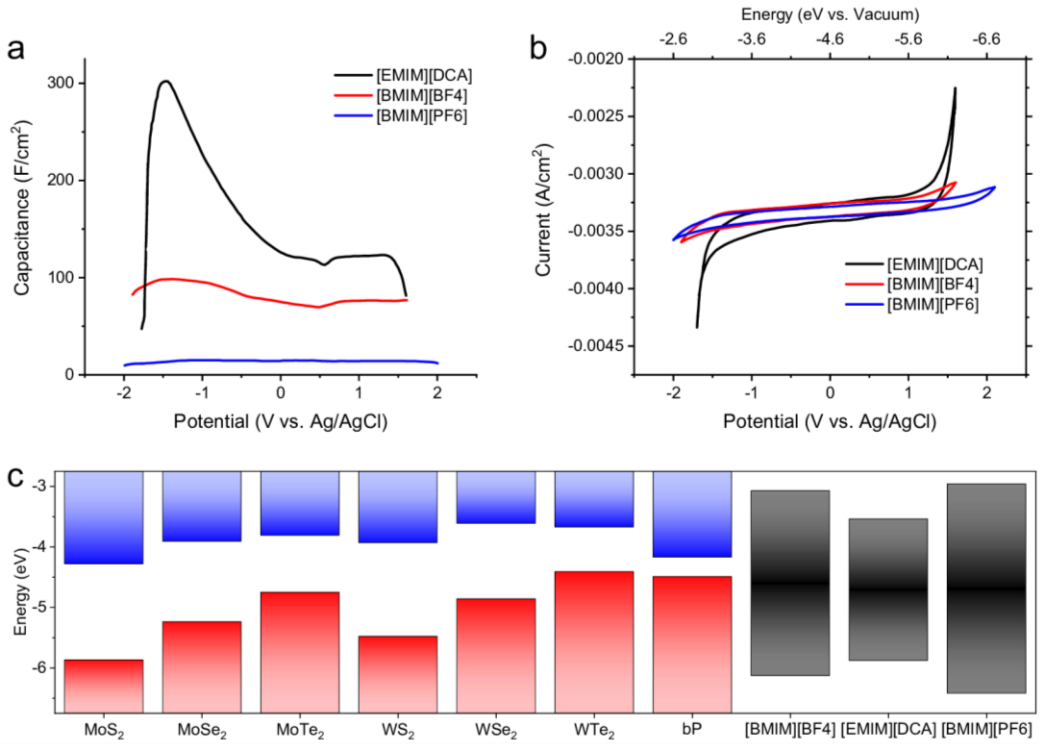

Figure 2.5. Band alignment of 2D materials and ionic electrolytes. a, b. the potential dependent areal capacitances at 5 Hz (a) and CV curves at 10 mV/s (b) of [EMIM][DCA], [BMIM][BF4], and [BMIM][PF6]. **c.** The band alignment of monolayered MoS_2, $MoSe_2$, $MoTe_2$, WS_2, WSe_2, and WTe_2 and bulk black phosphorous to the measured electrochemical stability windows of [BMIM][BF4], [EMIM][DCA], and [BMIM][PF6]. The band edges of the monolayer 2D materials are obtained from calculation results [39,40]. The band positions of bulk black phosphorous are measured by EQCS.

2.5 Conclusion

In conclusion, we have developed and employed an electrochemical method for measuring the DOS of 2D materials in ambient conditions. This versatile technique facilitates the facile characterization of the evolution of the DOS of a material subjected to mechanical strain and during chemical reactions. It also allows for the direct characterization of the electronic structure of 2D materials on insulating substrates, such as SiO_2/Si, which can remove the influence of surface potential and dielectric screening effects. Therefore, carrier energy and transport properties of devices can be directly obtained. This work paves the way for an extendable and *in-situ* electrochemical platform to capture the electronic structure of 2D materials and its dependence on defects, layer thickness, and substrate.

2.6 References

1 Zhang, S. *et al.* Defect structure of localized excitons in a WSe_2 monolayer. *Physical Review Letters* **119**, 046101 (2017).

2 Lu, C.-P., Li, G., Mao, J., Wang, L.-M. & Andrei, E. Y. Bandgap, mid-gap states, and gating effects in MoS_2. *Nano Letters* **14**, 4628-4633 (2014).

3 Liu, Y. *et al.* Gate-tunable giant stark effect in few-layer black phosphorus. *Nano Letters* **17**, 1970-1977 (2017).

4 Amani, M. *et al.* Near-unity photoluminescence quantum yield in MoS_2. *Science* **350**, 1065-1068 (2015).

5 Jaramillo, T. F. *et al.* Identification of active edge sites for electrochemical H_2 evolution from MoS_2 nanocatalysts. *Science* **317**, 100-102 (2007).

6 Ye, G. *et al.* Defects engineered monolayer MoS_2 for improved hydrogen evolution reaction. *Nano Letters* **16**, 1097-1103 (2016).

7 Ugeda, M. M. *et al.* Giant bandgap renormalization and excitonic effects in a monolayer transition metal dichalcogenide semiconductor. *Nature Materials* **13**, 1091-1095 (2014).

8 Li, H. *et al.* Imaging moiré flat bands in three-dimensional reconstructed WSe_2/WS_2 superlattices. *Nature Materials*, 1-6 (2021).

9 Jin, W. *et al.* Direct measurement of the thickness-dependent electronic band structure of MoS_2 using angle-resolved photoemission spectroscopy. *Physical Review Letters* **111**, 106801 (2013).

10 Ugeda, M. M. *et al.* Observation of topologically protected states at crystalline phase boundaries in single-layer WSe_2. *Nature Communications* **9**, 1-7 (2018).
11 Li, J. & Burke, P. J. Measurement of the combined quantum and electrochemical capacitance of a carbon nanotube. *Nature Communications* **10**, 1-9 (2019).
12 Pak, A. J., Paek, E. & Hwang, G. S. Relative contributions of quantum and double layer capacitance to the supercapacitor performance of carbon nanotubes in an ionic liquid. *Physical Chemistry Chemical Physics* **15**, 19741-19747 (2013).
13 Li, J., Pham, P. H., Zhou, W., Pham, T. D. & Burke, P. Carbon-nanotube–electrolyte interface: Quantum and electric double layer capacitance. *ACS Nano* **12**, 9763-9774 (2018).
14 Luryi, S. Quantum capacitance devices. *Applied Physics Letters* **52**, 501-503 (1988).
15 Miranda, D. A. & Bueno, P. R. Density functional theory and an experimentally-designed energy functional of electron density. *Physical Chemistry Chemical Physics* **18**, 25984-25992 (2016).
16 Ong, S. P., Andreussi, O., Wu, Y., Marzari, N. & Ceder, G. Electrochemical windows of room-temperature ionic liquids from molecular dynamics and density functional theory calculations. *Chemistry of Materials* **23**, 2979-2986 (2011).
17 Fedorov, M. V. & Kornyshev, A. Ionic liquids at electrified interfaces. *Chemical Reviews* **114**, 2978-3036 (2014).
18 Zhang, C., Johnson, A., Hsu, C.-L., Li, L.-J. & Shih, C.-K. Direct imaging of band profile in single layer MoS_2 on graphite: quasiparticle energy gap, metallic edge states, and edge band bending. *Nano Letters* **14**, 2443-2447 (2014).
19 Lee, W. *et al.* Time-resolved ARPES Determination of a Quasi-Particle Band Gap and Hot Electron Dynamics in Monolayer MoS_2. *Nano Letters* (2021).
20 Yang, G. *et al.* Possible Luttinger liquid behavior of edge transport in monolayer transition metal dichalcogenide crystals. *Nature Communications* **11**, 1-7 (2020).
21 Splendiani, A. *et al.* Emerging photoluminescence in monolayer MoS_2. *Nano letters* **10**, 1271-1275 (2010).
22 Yoon, Y., Ganapathi, K. & Salahuddin, S. How good can monolayer MoS_2 transistors be? *Nano Letters* **11**, 3768-3773 (2011).
23 Ponomarev, E. *et al.* Hole transport in exfoliated monolayer MoS_2. *ACS Nano* **12**, 2669-2676 (2018).
24 Liu, M. *et al.* Temperature-triggered sulfur vacancy evolution in monolayer MoS_2/graphene heterostructures. *Small* **13**, 1602967 (2017).
25 Mak, K. F., Lee, C., Hone, J., Shan, J. & Heinz, T. F. Atomically thin MoS 2: a new direct-gap semiconductor. *Physical review letters* **105**, 136805 (2010).
26 Dai, X. *et al.* Benchmark Investigation of Band-Gap Tunability of Monolayer Semiconductors under Hydrostatic Pressure with Focus-On Antimony. *Nanomaterials* **10**, 2154 (2020).
27 Xiao, H., Tahir-Kheli, J. & Goddard III, W. A. Accurate band gaps for semiconductors from density functional theory. *The Journal of Physical Chemistry Letters* **2**, 212-217 (2011).
28 Rivera, P. *et al.* Valley-polarized exciton dynamics in a 2D semiconductor heterostructure. *Science* **351**, 688-691 (2016).
29 Xiao, S.-L., Yu, W.-Z. & Gao, S.-P. Edge preference and band gap characters of MoS_2 and WS_2 nanoribbons. *Surface Science* **653**, 107-112 (2016).

30 Schweiger, H., Raybaud, P., Kresse, G. & Toulhoat, H. Shape and edge sites modifications of MoS_2 catalytic nanoparticles induced by working conditions: a theoretical study. *Journal of Catalysis* **207**, 76-87 (2002).
31 Feng, L.-p., Su, J., Chen, S. & Liu, Z.-t. First-principles investigations on vacancy formation and electronic structures of monolayer MoS_2. *Materials Chemistry Physics* **148**, 5-9 (2014).
32 Zhu, D. *et al.* Capture the growth kinetics of CVD growth of two-dimensional MoS_2. *npj 2D Materials and Applications* **1,** (2017).
33 Ast, C. R. *et al.* Sensing the quantum limit in scanning tunnelling spectroscopy. *Nature Communications* **7**, 1-8 (2016).
34 Zahid, F., Liu, L., Zhu, Y., Wang, J. & Guo, H. A generic tight-binding model for monolayer, bilayer and bulk MoS_2. *AIP Advances* **3**, 052111 (2013).
35 Li, H. *et al.* Kinetic study of hydrogen evolution reaction over strained MoS2 with sulfur vacancies using scanning electrochemical microscopy. *Journal of the American Chemical Society* **138**, 5123-5129 (2016).
36 Hinnemann, B. *et al.* Biomimetic hydrogen evolution: MoS2 nanoparticles as catalyst for hydrogen evolution. *Journal of the American Chemical Society* **127**, 5308-5309 (2005).
37 Zhou, Y. *et al.* Enhanced performance of in-plane transition metal dichalcogenides monolayers by configuring local atomic structures. *Nature Communications* **11**, 1-8 (2020).
38 Postorino, S. *et al.* Strain-induced effects on the electronic properties of 2D materials. *Nanomaterials and Nanotechnology* **10**, 1847980420902569 (2020).
39 Kang, J., Tongay, S., Zhou, J., Li, J. & Wu, J. Band offsets and heterostructures of two-dimensional semiconductors. *Applied Physics Letters* **102**, 012111 (2013).
40 Liu, Y., Stradins, P. & Wei, S.-H. Van der Waals metal-semiconductor junction: Weak Fermi level pinning enables effective tuning of Schottky barrier. *Science Advances* **2**, e1600069 (2016).
41 Das, S. *et al.* Tunable transport gap in phosphorene. *Nano Letters* **14,** 5733–5739 (2014).
42 Eaton, Peter, and Paul West. Atomic force microscopy. (Oxford university press, 2010)
43 Kresse, G. & Furthmuller, J. Efficient iterative schemes for ab initio total-energy calculations using a plane-wave basis set. *Phys. Rev. B* **54**, 11169–11186 (1996).
44 Kresse, G. & Furthmuller, J. Efficiency of ab-initio total energy calculations for metals and semiconductors using a plane-wave basis set. *Comput. Mater. Sci.,* **6**, 15–50 (1996).
45 Kresse, G. & Joubert, D. From ultrasoft pseudopotentials to the projector augmented-wave method. *Phys. Rev. B* **59**, 1758–1775 (1999).
46 Perdew, J. P., Burke, K. & Ernzerhof, M. Generalized gradient approximation made simple. *Phys. Rev. Lett.* **77**, 3865–3868 (1996).
47 Grimme, S., Antony, J., Ehrlich, S. & Krieg, H. A consistent and accurate ab initio parametrization of density functional dispersion correction (DFT-D) for the 94 elements H-Pu. *J. Chem. Phys.* **132**, 154104 (2010).

2.7 Acknowledgments:

Funding: This research was funded by U.S. Department of Energy, Office of Science, Basic Energy Sciences, Division of Materials Sciences and Engineering, under Award KC020105-FWP12152 Pacific Northwest National Laboratory (PNNL) was operated by Battelle for the Department of Energy under contract no. DE-AC05-76RLO1830. J. H. acknowledges the support of University of Washington Molecular Engineering Materials Center (MEM·C) NSF grant DMR-1719797. This material is based in part upon work supported by the state of Washington through the University of Washington Clean Energy Institute. Part of this work was conducted at the Washington Nanofabrication Facility / Molecular Analysis Facility, a National Nanotechnology Coordinated Infrastructure (NNCI) site at the University of Washington with partial support from the National Science Foundation via awards NNCI-1542101 and NNCI-2025489.

2.8 Supplementary Information

2.8.1 Determining the bandgap and the position of VBM and CBM of monolayer MoS_2 basal plane

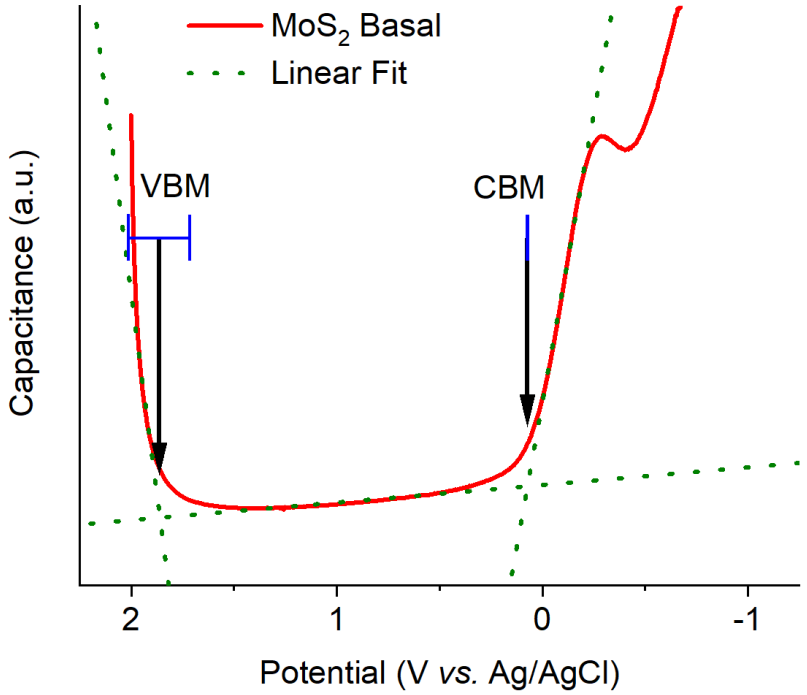

Figure 2.S1. Determining the VBM, CBM, and bandgap of MoS_2 basal plane. To find the valence and conduction band edges, a linear fit is applied to the near-linear regions of the QCS on the left-hand side, band gap, and right-hand side (green dotted lines). The VBM and CBM were determined as the x-coordinate of the intersection of the left-hand and band gap lines of fit and the right-hand and band gap lines of fit, respectively.

Linear Fit	VBM (line 1)	CBM (line 2)	Bandgap
Equation	$y_1 = m_1x_1 + b_1$	$y_1 = m_1x_1 + b_1$	$y_2 = m_2x_2 + b_2$
Intercept	-12.0 ± 0.8	1.288 ± 0.004	0.934 ± 0.002
Slope	6.9 ± 0.4	-4.98 ± 0.04	-0.076 ± 0.002
Residual Sum of Squares	0.019	0.0092	0.015
R-Square (COD)	0.96	0.99	0.91

Table 2.S1. Linear fitting parameters for the pristine 1-L MoS_2 EQCS Spectrum

If the equations for line 1 and line 2 are

$$y_1 = m_1x_1 + b_1$$

and

$$y_2 = m_2x_2 + b_2$$

The x-coordinate of the point of intersection is found by setting $y_1 = y_2$.

$$m_1x + b_1 = m_2x + b_2$$

Rearranging to solve for x gives

$$x = \frac{b_2 - b_1}{m_1 - m_2}$$

The error in x is calculated using the Gaussian propagation of error method using the equation

$$\sigma_x = \sqrt{\frac{dx}{db_1}^2 {\sigma_{b_1}}^2 + \frac{dx}{db_2}^2 {\sigma_{b_2}}^2 + \frac{dx}{dm_1}^2 {\sigma_{m_1}}^2 + \frac{dx}{dm_2}^2 {\sigma_{m_2}}^2}$$

The standard error in the fitting parameters is calculated automatically by the fitting routine.

The band gap is then calculated as the difference between the CBM and VBM.

$$Bandgap = CBM - VBM$$

The error in the bandgap is calculated using the Gaussian propagation, with the formula being,

$$\sigma_x = \sqrt{{\sigma_{CBM}}^2 + {\sigma_{VBM}}^2}$$

The calculated values are summarized in the table below.

VBM	CBM	Bandgap
1.86 ± 0.15 V	0.072 ± 0.001 V	1.79 ± 0.15 V

Table 2.S2. Extracted band edge positions and bandgap.

2.8.2 Additional electrochemical measurements

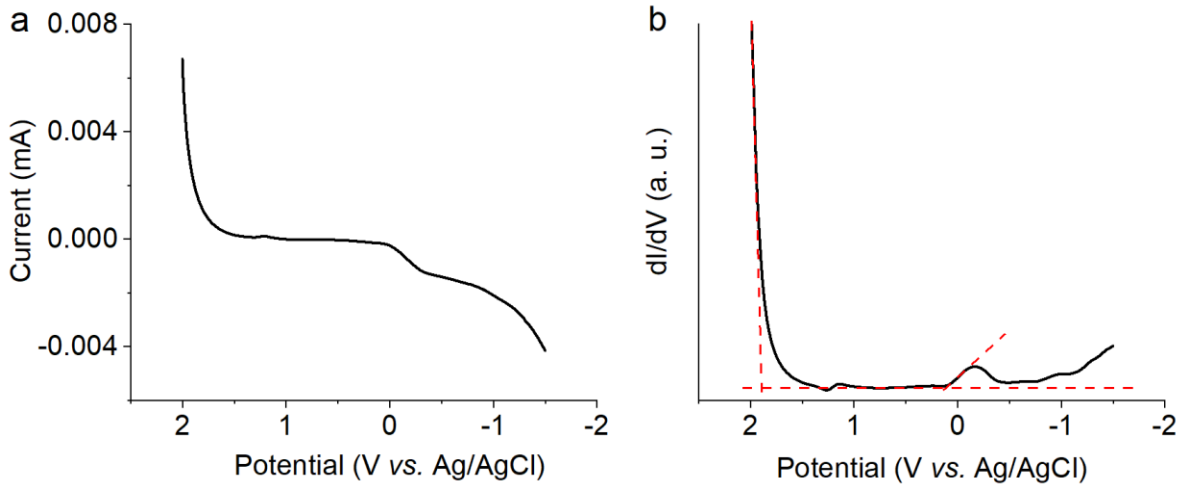

Figure 2.S2. a. The electrochemical tunneling current as a function of the applied potential. **b.** The dI/dV-V spectrum corresponding to the I-V spectrum shown in Figure 2.S1a.

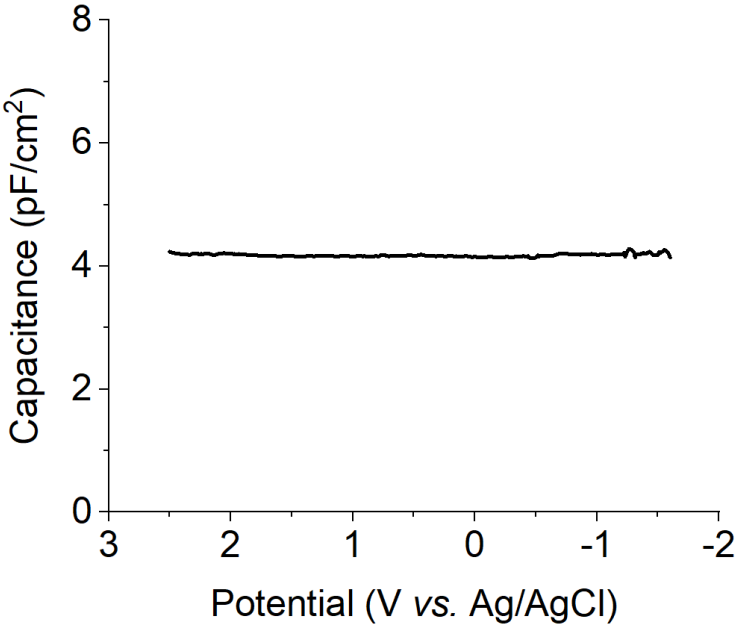

Figure 2.S3. The electrochemical capacitance of the PMMA insulating layer at 5 Hz. To evaluate the contribution of PMMA in the quantum capacitance measurement, a bilayer PMMA is spin-coated on a pre-made Ti/Au (5 nm/50 nm) coated silicon wafer and dried at 180°C. The capacitance of PMMA is around 4 pF/cm^2 in a wide potential range of -1.6 to 2.5 V *vs.* Ag/AgCl. It is much smaller than the capacitance of MoS_2 (as shown in Figure 1b), thus contributes little to the measured quantum capacitance. Different from the quantum capacitance spectra of MoS_2, no obvious peak is observed for the PMMA layer.

2.8.3 Computational details

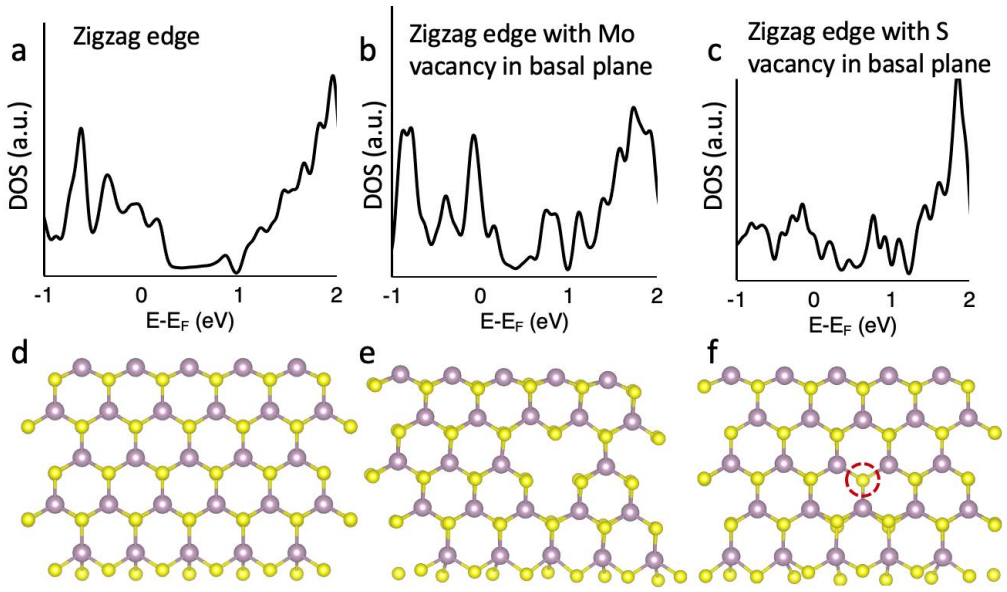

Figure 2.S4. Calculated DOS of single-layer MoS_2 ribbons with zigzag edges. a. DOS of stoichiometric ribbon; **b.** DOS of the ribbon with Mo vacancy in the basal plane, and (c) DOS of the ribbon with S vacancy in the basal plane. **d-f.** The corresponding optimized structures. The red circle in **f.** denotes the position of S vacancy.

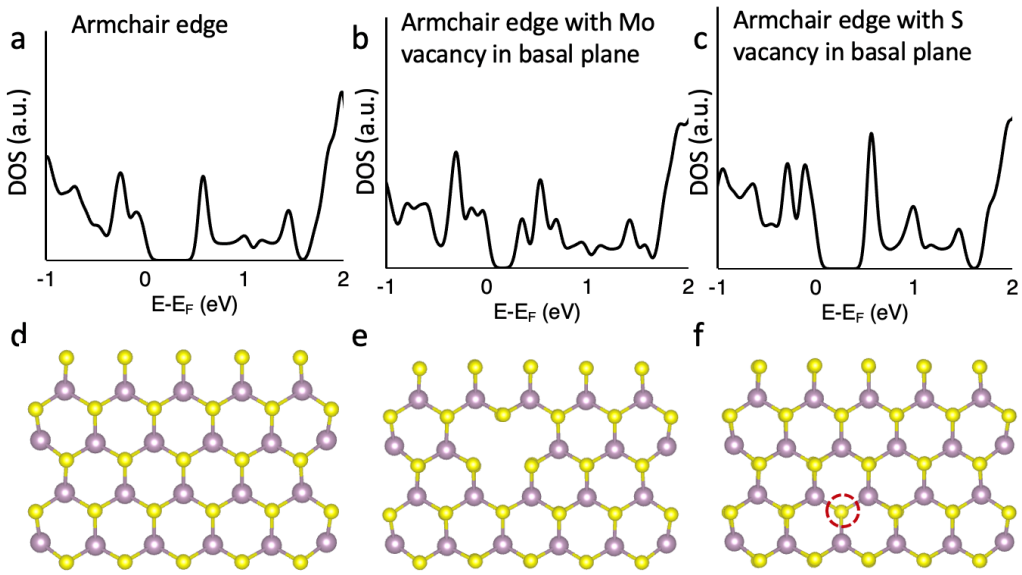

Figure 2.S5. Calculated DOS of single-layer MoS_2 ribbons with armchair edges. a. DOS of stoichiometric ribbon; **b.** DOS of the ribbon with Mo vacancy in the basal plane, and **c.** DOS of the ribbon with S vacancy in the basal plane. **d-f.** The corresponding optimized structures. The red circle in **f.** denotes the position of S vacancy.

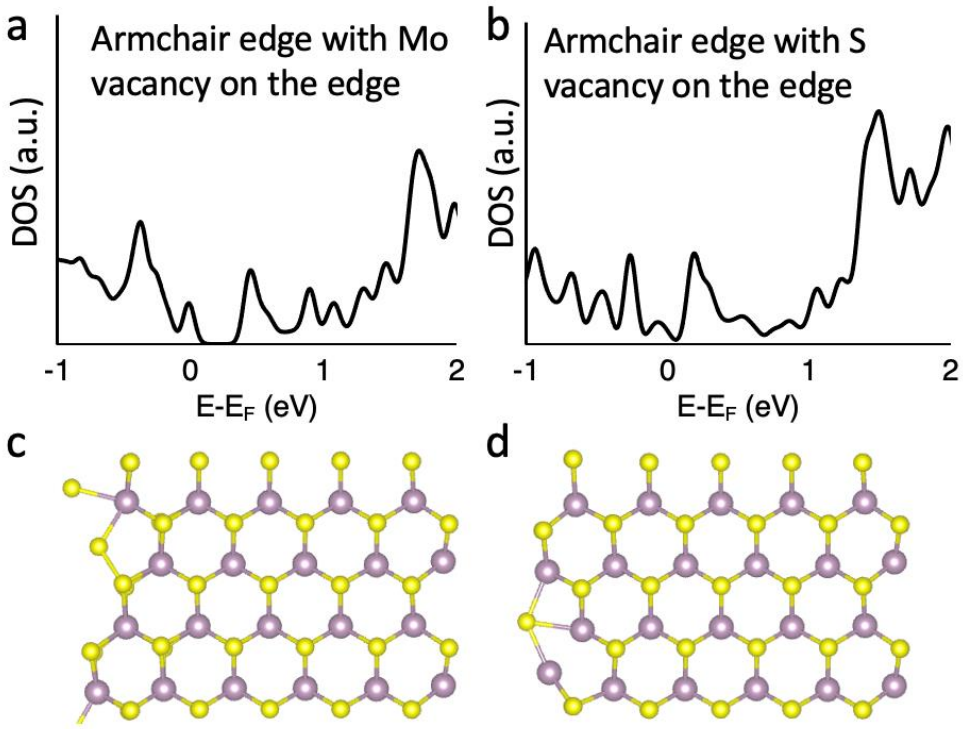

Figure 2.S6. Calculated DOS of single-layer MoS_2 ribbons with armchair edges. a. DOS of the ribbon with Mo vacancy at the edge, and **b.** DOS of the ribbon with S vacancy at the edge. **c-d.** The corresponding optimized structures.

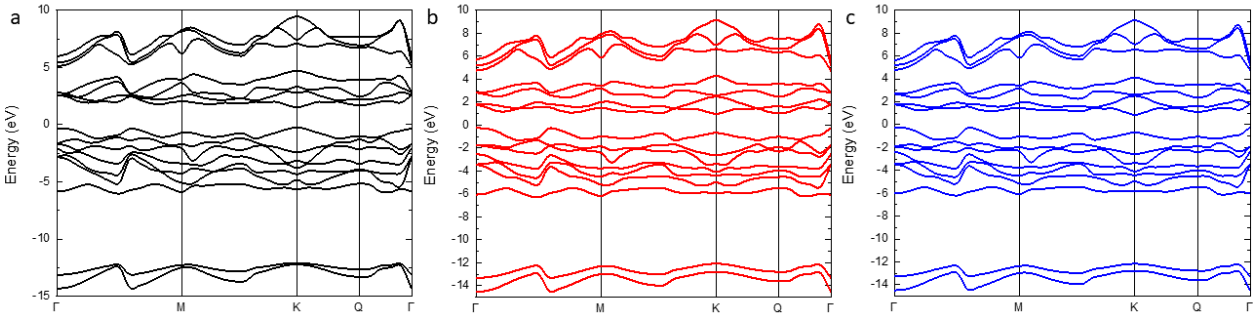

Figure 2.S7. Calculated band structures of single-layer MoS_2 slabs under strain. a. 0% biaxial strain, **b.** 1% biaxial strain, and **c.** 2% biaxial strain. The Fermi energy is shifted to 0 eV.

Second harmonic generation (SHG) spectroscopy

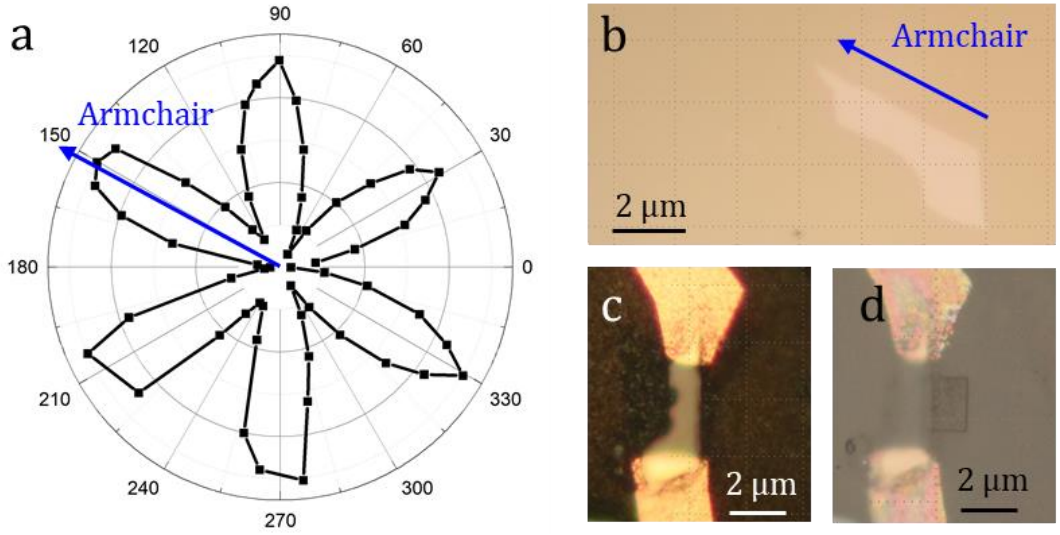

Figure 2.S8. SHG to identify edge direction. a. The resonant SHG intensity parallel to the incident laser polarization as a function of the laser polarization angle. **b-d.** The microscope images of the monolayer MoS_2 and the fabricated device. The armchair (blue arrow) edge of the monolayer sample is determined by the SHG.

2.8.5 Determination of the energetic resolution of the EQCS technique

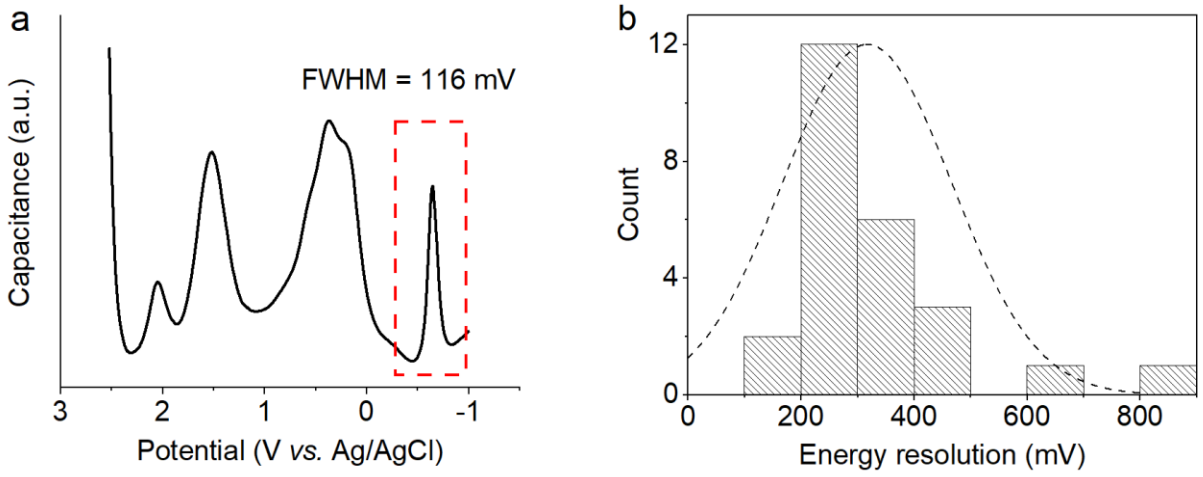

Figure 2.S9. Determination of the energetic resolution of the EQCS technique. a. One of the peaks in the MoS_2 electrochemical capacitance spectrum (framed in red) has an FWHM of 116 mV. **b.** The FWHMs of 25 peaks in the 5 electrochemical capacitance spectra are measured and summarized. The mean energy resolution is 317 mV, the highest is 116 mV.

2.8.6 Quantifying Strain Using Raman Spectroscopy

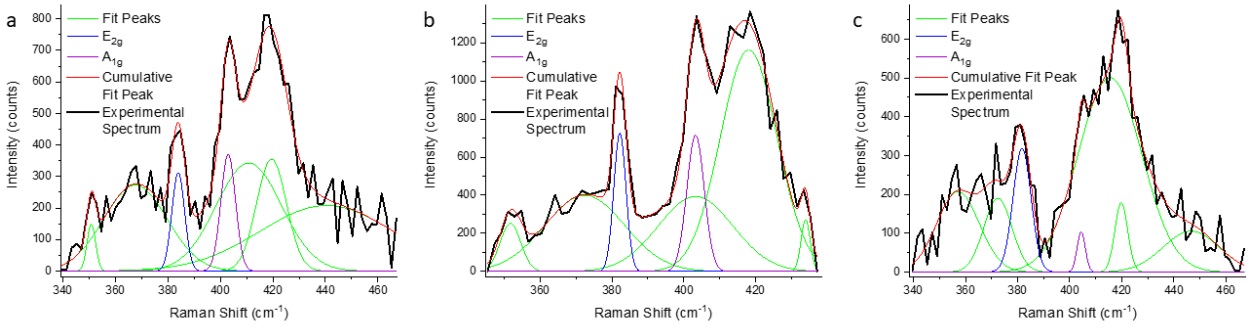

Figure 2.S10. Raman spectra with linear baseline subtraction and Gaussian peak fitting to quantify the strain felt by the monolayer MoS_2 flake. Spectra when the flake is **a.** unstrained,

b. under intermediate strain, and **c.** under high strain. The color of each curve corresponds to the entry in the legend. The green curves are contributed by the polyimide and PET substrates and the cyanoacrylate glue.

Expected Biaxial Strain	Gaussian Fit	E_{2g}	A_{1g}
0% Strain	Equation	$y = \frac{Ae^{\frac{-4\ln(2)(x-x_c)^2}{w^2}}}{w\sqrt{\frac{\pi}{4\ln(2)}}}$	$y = \frac{Ae^{\frac{-4\ln(2)(x-x_c)^2}{w^2}}}{w\sqrt{\frac{\pi}{4\ln(2)}}}$
	A	1909.1 ± 591.4	2572.6 ± 1453.2
	x_c	384.0 ± 0.45	403.0 ± 0.5
	w	5.7 ± 1.3	6.5 ± 1.9
	R-Square (COD)	0.9457	
	Residual Sum of Squares	155557	
1% Strain	Equation	$y = \frac{Ae^{\frac{-4\ln(2)(x-x_c)^2}{w^2}}}{w\sqrt{\frac{\pi}{4\ln(2)}}}$	$y = \frac{Ae^{\frac{-4\ln(2)(x-x_c)^2}{w^2}}}{w\sqrt{\frac{\pi}{4\ln(2)}}}$
	A	3088.3 ± 619.8	4364.8 ± 1589.8
	x_c	382.2 ± 0.2	403.3 ± 0.3

	w	4.0 ± 0.6	5.7 ± 1.0
	R-Square (COD)	0.9807	
	Residual Sum of Squares	148835	
2% Strain	Equation	$y = \frac{Ae^{\frac{-4\ln(2)(x-x_c)^2}{w^2}}}{w\sqrt{\frac{\pi}{4\ln(2)}}}$	$y = \frac{Ae^{\frac{-4\ln(2)(x-x_c)^2}{w^2}}}{w\sqrt{\frac{\pi}{4\ln(2)}}}$
	A	2761.5 ± 2581.4	408.6 ± 290.7
	x_c	381.7 ± 1.6	404.4 ± 0.9
	w	8.1 ± 2.6	3.7 ± 2.6
	R-Square (COD)	0.9343	
	Residual Sum of Squares	118079	

Table 2.S3. Fitting parameters of the 1-L MoS_2 Raman spectrum

Ordinarily, strain can be extracted from the shift of the E^1_{2g} or A_{1g} peak position under strain from its unstrained position using a calibration factor[S1]. However, for these measurements, an arbitrary linear baseline was applied during the Gaussian peak fitting. This means that the absolute peak position can no longer be used to quantify strain. Instead, the separation between the E^1_{2g} and A_{1g} peaks, $\Delta\vartheta$, can be used. The difference between the two peaks is given by:

$$\Delta\vartheta_{unstrained} = \vartheta_{A_{1g}} - \vartheta_{E^1_{2g}}$$

Where ϑ is the peak position of the mode given in the subscript. Under strain, the E^1_{2g} peak red shifts at a faster rate than the A_{1g} peak so that the peak separation increases. This increased separation can be quantified as:

$$\Delta\vartheta_{strained} = \Delta\vartheta_{unstrained} + (\delta\vartheta_{E^1_{2g}} - \delta\vartheta_{A_{1g}})$$

Where $\delta\vartheta$ is the shift with strain from the unstrained peak position of the mode in the subscript. $\delta\vartheta$ is related to the strain by the rate of peak shift per stain percent for the appropriate Raman mode:

$$\delta\vartheta = rate \times x$$

This rate is calibrated experimentally and can be found in the literature. Substituting the third expression into the second gives:

$$\Delta\vartheta_{strained} = \Delta\vartheta_{unstrained} + (rate_{E^1_{2g}} \times x - rate_{A_{1g}} \times x)$$

Rearranging to solve for x gives:

$$x = \frac{\Delta\vartheta_{strained} - \Delta\vartheta_{unstrained}}{rate_{E^1_{2g}} - rate_{A_{1g}}}$$

Where x is the strain. For this work, $rate_{E^1_{2g}}$ and $rate_{A_{1g}}$ are equal to the literature values 4.48 $cm^{-1}/\%$ and 1.02 $cm^{-1}/\%$, respectively[S7]. The extracted values of strain are given in the table below.

Expected Biaxial Strain	0%	1%	2%
Measured Biaxial Strain	0%	0.6 ± 0.2 %	1.0 ± 0.6 %

Table 2.S4. Expected strain and real strain extracted from the Raman spectra of the MoS_2 flake under biaxial strain

2.8.7 EQCS measurement of black phosphorous

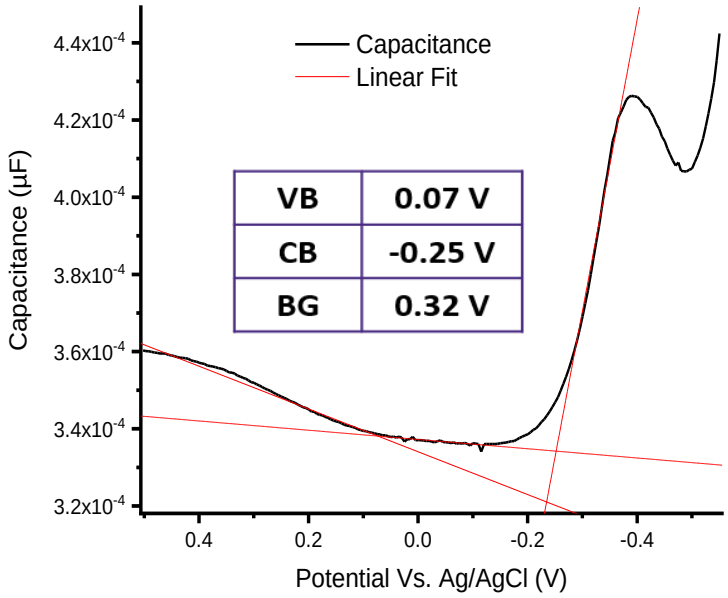

Figure 2.S11. Electrochemical quantum capacitance spectra of bulk black phosphorous. The extracted VBM, CBM, and BG for each material are shown in the inset tables. Notably, the extracted values for the bandgap of bulk black phosphorous matches well with the literature value of ~0.3[S2] eV.

2.8.8 References

S1 Li, H. *et al.* Kinetic study of hydrogen evolution reaction over strained MoS_2 with sulfur vacancies using scanning electrochemical microscopy. *Journal of the American Chemical Society* **138**, 5123-5129 (2016).

S2 Das, S. *et al.* Tunable transport gap in phosphorene. *Nano Letters* **14,** 5733–5739 (2014).

3 CHARACTERIZATION OF THE EVOLVING ROLE OF DEFECTS IN DETERMINING THE ELECTRONIC STRUCTURE AND ELECTROCHEMICAL BEHAVIOR OF MONOLAYER MOS_2

Significant portions of this chapter are adapted from:

Mitchell Kaiser, Hao Tang, Jose Ortiz-Garcia, Maria Sushko, Shuai Zhang, Ying Xia, Yuhuan Meng, Zbynek Novotny, Zdenek Dohnalek, Jun Liu. Characterization of the Evolving Role of Defects in Determining the Electronic Structure and Electrochemical Behavior of Monolayer MoS_2. In preparation.

Note for collaborative work: Conductive AFM images were captured by Professor Shuai Zhang. PL spectra were measured by Yuhuan Meng. XPS results were collected by Doctor Zdenek Novotny and Doctor Jose Ortiz-Garcia. Computations were performed by Doctor Maria Sushko.

3.1 Abstract

Two-dimensional van der Waals materials are promising materials for heterogeneous catalysis because of their exceptionally large surface area to volume and mass ratios, and their relatively low cost. In particular, monolayer molybdenum sulfide (1-L MoS_2) has been extensively studied as an electrocatalyst for the hydrogen evolution reaction (HER). Previous studies have identified the native sulfur vacancies as the catalytically active sites on the basal plane and shown that increasing the vacancy concentration can result in an increase in catalytic performance. This is generally believed to be due to the stabilization of adsorbed hydrogen on the MoS_2 surface by the creation of a more favorable electronic structure in the monolayer, which lowers the barrier for

HER. However, these studies fail to provide experimental evidence to demonstrate electronic structure modification by these vacancies, or even images of the vacancies themselves. These studies also focus on the initial cycles of HER, and therefore fail to understand the behavior of this material with time, or to identify its failure mechanism. Here, long-duration electrocatalytic experiments allow us to assess the change in the functional properties of the 1-L MoS_2 electrocatalyst with time. The novel electrochemical quantum capacitance spectroscopy technique (EQCS) developed by our group allows us to measure the change in the electronic structure of the catalyst with time. Conductive AFM images of the material and XPS measurements at different time steps allow us to capture the evolution of the vacancy structure and concentration. Taken together with computational modeling, this information provides experimental evidence for the modification of the 1-L MoS_2 electronic structure and functional properties by the inclusion of defects. We find that individual sulfur vacancies promote catalytic activity through the hydrogen binding energy effect and identify the ideal defect structure for HER. In addition, we identify the failure mechanism of the single-layer catalyst. These results have implications not only for the design of HER catalysts, but also for a method to develop design rules for the rational design of functional materials.

3.2 Introduction

The manipulation and isolation of single-layer graphene by mechanical exfoliation of graphite ignited a fervor of research to understand the unique thermal, mechanical, and electronic properties of this dimensionally-confined material[1]. Massive research interest was simultaneously generated in discovering and understanding a host of other two-dimensional (2D) materials that could also be isolated by mechanical exfoliation[2]. Although research on monolayer graphene has rapidly

reached maturity, there are hundreds of other candidate 2D materials, many of which have yet to be fully explored. Moreover, a nearly infinite phase space becomes available for new materials design upon mixing and matching these materials into novel heterostructures.

A cornucopia of 2D materials exist, including transition metal dichalcogenides whose various symmetries and atomic combinations result in permutations that are semi-conducting, metallic, superconducting, and even Weyl semimetals[3]. There are also 2D insulators, such as hexagonal boron nitride, ferromagnets like CrI_3 and Fe_3GeTe_2, topological insulators like monolayer WTe_2 and ferroelectrics, which include the binary oxides of ZrO_2 and HfO_2[4, 5]. An additional level of functionality is added by the rich variety of defects possible in these materials. Examples are substitutional impurities, vacancies, grain boundaries, and adatoms[4]. Considering that nearly every unique combination of these factors results in a material with a new property, the value of studying these materials is clear[6-8].

Furthermore, 2D materials have garnered interest for catalytic applications owing to their high surface area to volume and surface area to mass ratios[9]. For heterogenous catalysis where the reactant adsorbs to the surface of the catalyst, such as the case of protons in the hydrogen evolution reaction, an important criterion for a good catalyst is that the free energy of the adsorbed species is close to that of the reactant and product[10]. This requires overlap of the density of states of the adsorbate and active sites on the catalyst[11]. In a 2D catalyst, the energy of these states can be readily tuned via surface functionalization, effectively modulating the adsorption energy[12].

Monolayer molybdenum disulfide (1-L MoS_2) is a prime example of such a catalyst. It has been shown to be a favorable candidate to replace platinum as an electrocatalyst for the hydrogen evolution reaction (HER); a promising method of converting electricity from renewable energy sources into fuel[4,13]. Sulfur vacancies, native defects which have an intrinsic concentration of

approximately 5×10^{12} - 5×10^{13} per square centimeter, act as the catalytically active sites on the otherwise chemically inert basal plane of this material[14]. Increasing the number of sulfur vacancies above this intrinsic value enhances the catalytic activity of 1-L MoS_2 for HER. Various strategies have been employed to generate sulfur vacancies, including electrochemical desulfurization, plasma treatment, and salt-assisted chemical vapor deposition[15,16]. These studies have demonstrated that increasing the number of sulfur vacancies not only increases the number of active sites, but also lowers the free energy of hydrogen adsorption, reducing the barrier toward[17]. The reduction of the free energy is a result of undercoordinated molybdenum d-orbitals, which produce a peak in the density of states (DOS) that overlaps with the energy of proton s-orbitals.[18] While these methods have been successful in enhancing the catalytic performance of monolayer MoS_2, to create a stable catalyst with the highest possible performance necessitates an in-depth knowledge of defect states and the transformation of the electronic structure induced by chemical reactions under operating conditions. In fact, it has been observed by our group that simply performing HER with 1-L MoS_2 causes a change in the catalytic performance, and likely the electronic structure, with time. While plenty of theoretical literature exists on the effect of defects on the electronic structure of these materials, direct experimental measurement of the modified electronic structure is difficult. Traditional methods such as STS or ARPES require ultrahigh vacuum and extremely clean samples, which precludes their usage in electrochemical systems[19].

In this work, 1-L MoS_2 is investigated as an electrocatalyst for the hydrogen evolution reaction. The change in the catalytic activity over time is measured, and the novel electrochemical quantum capacitance spectroscopy (EQCS) technique developed by our group is used to measure the evolution of the electronic structure (DOS) over the course of the electrocatalytic measurements. We observe and increase, and then decrease in the HER electrocatalytic performance over time.

We hypothesize that this phenomenon is due to the initial formation of favorable single sulfur vacancies that increase the HER performance, but that with time and increasing sulfur vacancy concentration, these vacancies grow into clusters that decrease the catalytic activity[20]. While this changes the number of catalytically active sites, the most important effect of these vacancies is the modification of the MoS_2 electronic structure, which determines its functional properties. The objective of this work is to develop a link between defect structure and concentration with electronic structure and the electrochemical performance of the 2D TMD. By fully understanding these relationships, rational principles based on electronic structure for the design of low-dimensional functional materials can be developed. This has implications for practical device applications and presents an opportunity to explore fundamental phenomena.

3.3 Experimental

3.3.1 Optical microscopy

All optical micrographs were captured using a Nikon LVDIA-NDIA microscope in bright field mode.

3.3.2 Device fabrication

The microelectrochemical cells are fabricated using an identical method to our previous work (Chapter 2). Briefly, 1-L MoS_2 is mechanically exfoliated using scotch tape and isolated on a silicon wafer with a 285 nm wet thermal oxide coating. A suitable monolayer is identified using optical microscopy. The wafer chip containing the monolayer is then coated with PMMA electron

beam lithography resist, and electrodes are patterned using electron beam lithography. A 10 nm layer of titanium, followed by a 100 nm layer of gold, are deposited using electron beam evaporation. The device is placed in acetone for an hour to dissolve the PMMA, and if necessary, a transfer pipette is used to rinse away any remaining gold. The chip is then coated again with PMMA, and 3-by-3 micron window is patterned on the basal plane of MoS_2. An electrolyte holder is then glued onto the device. More details can be found in Chapter 2.

The devices used for the cAFM and XPS measurements were fabricated using the gold-assisted exfoliation technique. First, a 10 nm layer of titanium, then a 100 nm layer of gold are deposited on a silicon oxide coated silicon chip at a rate of 0.2 Å/s and 1 Å/s, respectively. Single-sided thermal release tape (TRT) with a release temperature of 110 ºC was pressed to a bulk crystal of MoS_2 and then peeled away, taking with it a thick crystal of MoS_2. The TRT containing the MoS_2 is then pressed onto the gold-coated chip, and then heated at 120 ºC for 2 minutes. Once the TRT tape was observed to completely peel away, it was removed, and the chip was allowed to cool for 10 minutes. The thick MoS_2 crystal that was deposited on the chip is then peeled away using Scotch tape, revealing large area mono and few-layers.

3.3.3 Confocal Raman Spectroscopy

Raman spectra were obtained using a Renishaw inVia Confocal Raman Microscope, which is equipped with a 532 nm laser, a 50x objective, and a 1200 l/mm grating. The laser power was set to 1%. Each spectrum was measured with 4 10-second accumulations, covering an extended range from 200 to 600 cm^{-1}.

3.3.4 Confocal photoluminescence spectroscopy

PL spectra were obtained using a Horiba LabRAM HR-800 Microscope, which is equipped with a 532 nm laser and a 50x objective, and a 150 l/mm grating. The confocal hole is set to 800 µm. The illumination intensity was 3 suns. Each spectrum was measured with 3 10-second accumulations at a central wavelength of 650 nm.

3.3.5 Second harmonic generation spectroscopy

The SHG spectra were measured using a home-made setup with a 50x objective and a 1080 nm laser. The power at the sample was 1 µW. The integration time was 2 seconds.

3.3.6 Electrochemical hydrogen evolution measurements

All electrochemical data was recorded using a BioLogic SP300 Potentiostat with an ultralow current cable. The microelectrochemical reactor was filled with a 0.5 M sulfuric acid electrolyte and the commercial Ag/AgCl reference electrode with saturated KCl (StonyLab) and graphitic carbon electrode (StonyLab) were inserted. 1-L MoS_2 was the working electrode, with contact established between the potentiostat and the device by touching a micromanipulator probe with a tungsten needle to the gold contact on the device. Prior to catalytic testing, the device is allowed to rest until the open circuit voltage stabilizes. This indicates any remaining surface contamination has been dissolved, and the electrochemical double-layer has reached equilibrium. Cyclic voltammetry with a scan window of 0.2 to -0.4 V V. Ag/AgCl with a scan rate of 5 mV/s was employed for the HER measurements.

The HER results shown here were measured on one device, while an identical device was subjected to the same catalytic cycling was used for the EQCS tests. This 2nd device was first measured by EQCS, rinsed with DI water, and then dried for an hour, before undergoing HER tests for a given number of cycles. Between each EQCS and HER step, the device was washed and dried using the same procedure. The experiment was conducted on 2 devices because the pauses in the HER testing result in small discontinuities in the cycling data, which confuse interpretation.

3.3.7 Electrochemical quantum capacitance spectroscopy measurements

The EQCS spectra were obtained by staircase electrochemical impedance spectroscopy using a 10 mV amplitude at a frequency of 5 Hz and a current range of 100 nA. The voltage window was chosen to ensure the band edges could be measured, but also so the current never exceeded the set current range. The step size between each point was 5 mV. The ionic liquid 1-butyl-3-methylimidazolium tetrafluoroborate ([BMIM][BF_4]) was used as the electrolyte. The monolayer flake was the working electrode, graphitic carbon the counter electrode, and Ag/AgCl with 0.1 M [BMIM][Cl] in [BMIM][BF_4] the reference electrode. More details, including the theory of the measurement, can be found in chapter 2.

3.3.8 Atomic force microscopy

3.3.8.1 Topographic imaging

The low magnification AFM image of the 2D MoS2 flake was obtained in air using amplitude modulation mode on a Bruker Multimode 8 AFM, equipped with RFESPA-75 probes from Bruker.

These probes generally have a resonance frequency of 75 kHz and a spring constant of 3 N/m. Data was processed offline using Gwyddion SPM data analysis software.

3.3.8.2 AFM cleaning

Prior to electrochemical testing, 1-L MoS_2 UME surfaces are cleaned in contact mode using an OTESPA-R3 probe from Bruker. The probe has a nominal spring constant and resonant frequency of 26 N/m and 300 kHz, respectively. The UME is located using tapping mode, and then the mode is changed to contact. Thermal tuning is used to extract the effective spring constant and deflection sensitivity. These values are used to calculate the deflection value that would result in a 100 nN force being applied by the tip. This value is then added to the free vertical deflection to determine the deflection setpoint. The scan rate is adjusted depending on the scan size so that the tip velocity is 1 um/sec, and the number of lines are determined by dividing the scan height by the tip radius. The scan is then started and is allowed to continue until the friction image becomes uniform, usually 3-4 scans.

3.3.8.3 cAFM

The cAFM characterization was performed using a Cypher ES AFM (Asylum Research, CA) in an N2 gas environment at room temperature. The CDT-CONTR AFM probes (NanoSensors) with doped-diamond-coating were used in the cAFM measurements. The spring constants, 0.95 ± 0.05 N/m, of the cantilevers were calibrated before each measurement. The AFM data was collected in contact mode with applied force between 4.0-10.0 nN to keep the contact between the AFM probes and the sample surfaces stable. Two biases, -400 mV and +400 mV, were applied to the samples during the measurement. The offline data processing was done with Gwyddion SPM data analysis software.

3.3.9 X-Ray photoelectron spectroscopy

XPS analysis was performed in an ultra-high vacuum (UHV, base pressure ~1 × 10−10 Torr) chamber containing an EA 125 electron analyzer (Omicron) and a non-monochromatized Al (Kα) x-ray source (SPECS). The measurements were performed at 300 K using 20 eV pass energy, 54.7° x-ray incidence and 0° electron emission angle with respect to the surface normal. The energy scale was calibrated by setting the Au4f7/2 line to 84.0 eV. Stoichiometric ratios of S:Mo were obtained for all devices after peak fitting of the Shirley background subtracted spectra in CasaXPS using sensitivity factors from Ref. (1). To facilitate comparison of Svac between samples, the pristine S:Mo ratio was set to 2 and propagated through the rest of the dataset.

3.3.10 Computational methods

Single-layer MoS_2 was modeled using 3D periodic model as 2D sheets periodic in the directions along the basal plane. A 15 Å vacuum gap between images of the basal planes was used to avoid interactions between periodic images. Point and extended S-defects were introduced in the basal plane. The 5 × 5 supercell was used to simulate 4% concentration of single vacancies. All atoms were fully relaxed during structural optimization. The convergence criterion for geometric relaxation was set to 0.01 eV/ Å.

Density functional theory (DFT) simulations of the electronic structure of MoS_2 sheets were performed using periodic plane wave DFT implemented in VASP code[44, 45]. Generalized gradient approximation and projected augmented wave (PAW) potentials[46] were used with PBE exchange-correlation functional[47] and the D2 Grimme dispersion correction[48]. Spin polarization was

included in all calculations: 6 × 6 × 1 Gamma centred Monkhorst–Pack grid was used for k-point sampling of the Brillouin zone. Plane wave cutoff of 400 eV was used.

A periodic slab model was used for hydrogen chemisorption calculations. A single-layer MoS_2 slab with 1 to 3 S-vacancies in the basal plane and hydrogen atoms decorating the vacancy was optimized using the convergence criterion of 0.01 eV/ Å. The free energy of the adsorbed state was calculated as

$$\Delta G = \Delta E_{H^*} - \Delta E_{ZPE} - T\Delta S_{H,}$$

where ΔE_{H^*} is the hydrogen chemisorption energy, and ΔE_{ZPE} is the difference of the zero-point energy between the adsorbed state and the gas phase. Considering that the vibrational entropy of H* in the adsorbed state is very small, the entropy of 1/2 H_2 adsorption, $\Delta S_{H,}$ can be approximated as 1/2 of the entropy of H_2 in the gas phase at standard conditions. The hydrogen chemisorption energy was calculated as

$$\Delta E_{H^*} = E(MoS_2+nH) - E(MoS_2+(n-1)H) - 1/2\ E(H_2),$$

where $E(MoS_2+nH)$ is the total DFT energy for the MoS_2 layer with n hydrogen atoms adsorbed on the S vacancy, $E(MoS_2+(n-1)H)$ is the total DFT energy for (n-1) hydrogen atoms adsorbed on the V_S and $E(H_2)$ is the DFT energy for a hydrogen molecule in the gas phase.

3.4 Results and Discussion

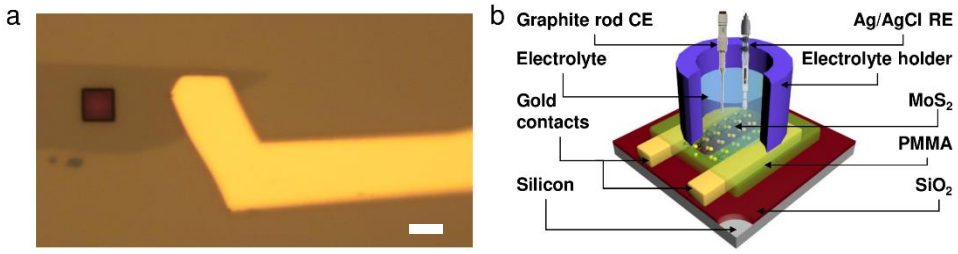

Figure 3.1. Device construction. a. Optical micrograph depicting the 1-L MoS_2 flake (grey-brown), gold contact (yellow), and ultramicroelectrode window (dark brown) used to expose only a 3-by-3 micron area of the basal plane. Scale bar: 3 microns. **b.** Schematic of the micro electrochemical reactor used for the HER and EQCS measurements. The electrolyte holder is glued to the device shown in **a**. The MoS_2 forms the working electrode, while a standard graphite rod and silver wire coated with silver chloride immersed in saturated potassium chloride form the counter and reference electrode, respectively.

Prior to device fabrication, 1-L MoS_2 flakes are obtained from mechanical exfoliation. Potential monolayers are first identified by color-contrast using optical lithography, and then characterized AFM, Raman spectroscopy, photoluminescence spectroscopy (PL), and second harmonic generation spectroscopy (SHG). Figure 3.2 shows these results for the device used for the EQCS measurement. The 19 cm^{-1} spacing between the E^1_{2g} and A_{1g} Raman peaks (Figure 3.2a), the 1.86 eV PL peak (Figure2b), the 6-fold symmetry in the SHG spectrum, and the ~0.75 nm thickness measured by AFM verify the flake is a single layer[21,22].

Figure 3.1a shows an optical micrograph of the monolayer 1-L MoS_2 device. PMMA is used to insulate the device from the electrolyte, and a small window is fabricated using electron beam lithography to define a 3-by-3 micron ultramicroelectrode (UME). Figure 3.1b shows a schematic

of the microelectrochemical reactor. Notably, a large electrolyte holder is glued to the UME device, enabling the use of a standard Ag/AgCl with saturated KCl reference and a graphite counter-electrode. This ensures a reliable measurement of the absolute potential of the UME working electrode, and sufficiently large counter-electrode capacitance, which is critical to the EQCS technique (chapter 2).

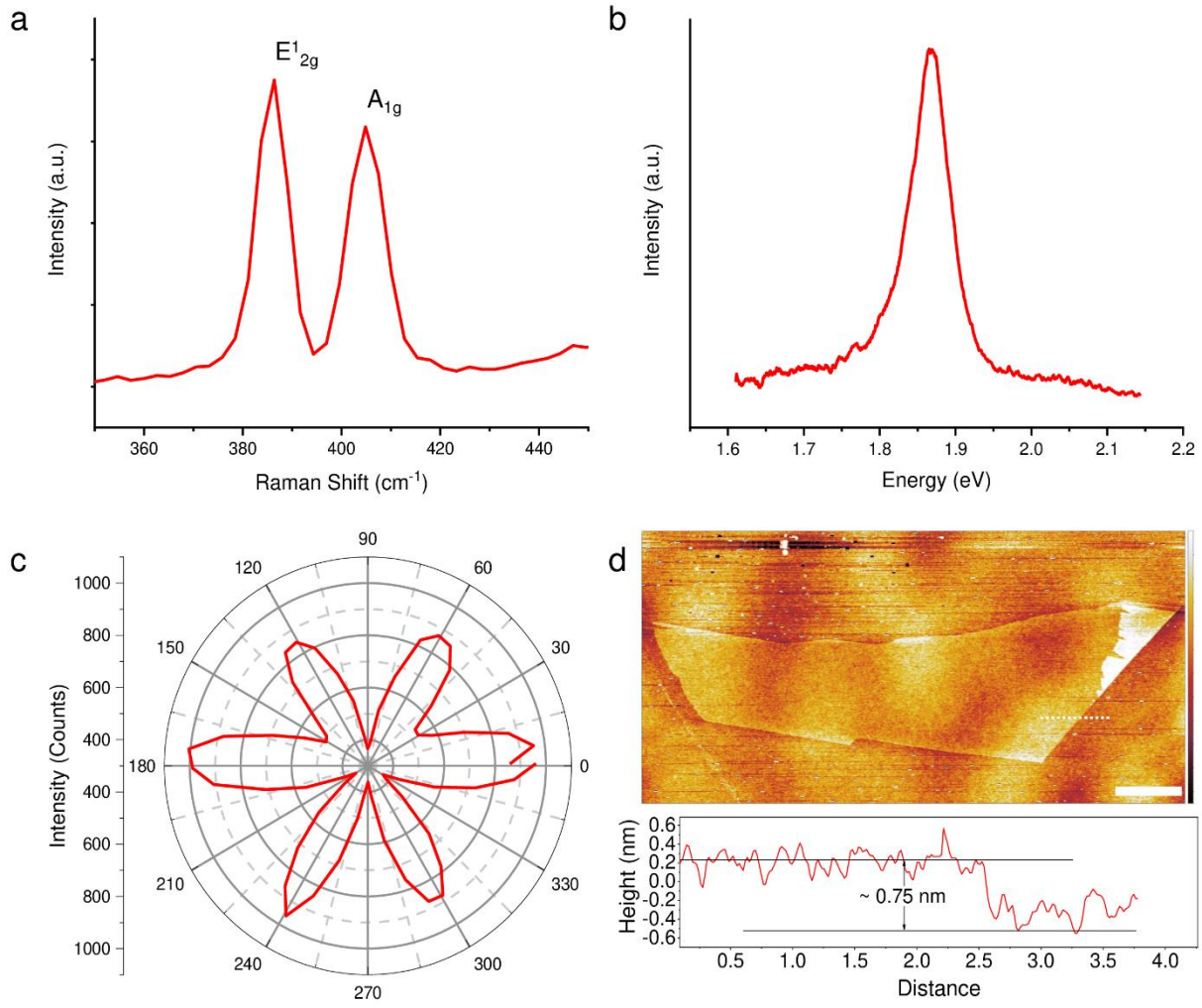

Figure 3.2. Characterization of 1-L MoS_2. a. Raman spectrum of 1-L MoS_2. The E^1_{2g} and A_{1g} peaks are separated by 19 cm^{-1}. Spectra was measured using a 532 nm laser at 1% power. **b**. Photoluminescence spectrum of 1-L MoS_2. The peak center is 1.86 eV. The spectrum was measured using a 532 nm laser under 3 sun illumination intensity. **c.** SHG spectrum of 1-L MoS_2.

The spectrum was measured using a 1080 nm laser with 1 μW power on the sample. **d.** AFM image of the 1-L MoS_2 flake. The dotted line shows where the height cross-section below the image was extracted. Scale bar: 4 microns. Height range (gradient): 2.3 nm.

The cyclic voltammetry data obtained during HER measurements is shown in Figure 3.3. The cyclic voltammograms do not show any peaks and have only a small capacitive component, as is expected of an UME with an appropriate scan rate (Figure 3.3a)[23]. Initially, the catalytic current increases in magnitude before reaching its maximum value at cycle 80. This effect could be attributed to contamination from the MoS_2 surface being cleaned away as the result of electrochemical processes. However, this explanation is negated by the fact that the ultramicroelectrode surface was first cleaned by scratching with an AFM tip and then left to soak in the sulfuric acid electrolyte for 2 hours prior to the start of the experiment, which should dissolve any remaining contamination[24,25]. From here, the current remains relatively stable until it begins to decay at cycle 140. Finally, the current plateaus around cycle 163.

To gain deeper insight into the catalytic performance of MoS_2 with time, Tafel analysis is performed on the HER cycling data. Cycles 1, 31, 80, and 171 are selected, as these correspond to the cycle number where EQCS is performed (Figure 4). The extracted Tafel slopes support the behavior observed in the cyclic voltammetry, showing a decrease in Tafel slope from cycle 1 to 80, indicating increased catalytic performance. The Tafel slope is seen to increase at cycle 171, showing a reduction in catalytic performance, which is in good agreement with the smaller current density observed in the cyclic voltammetry.

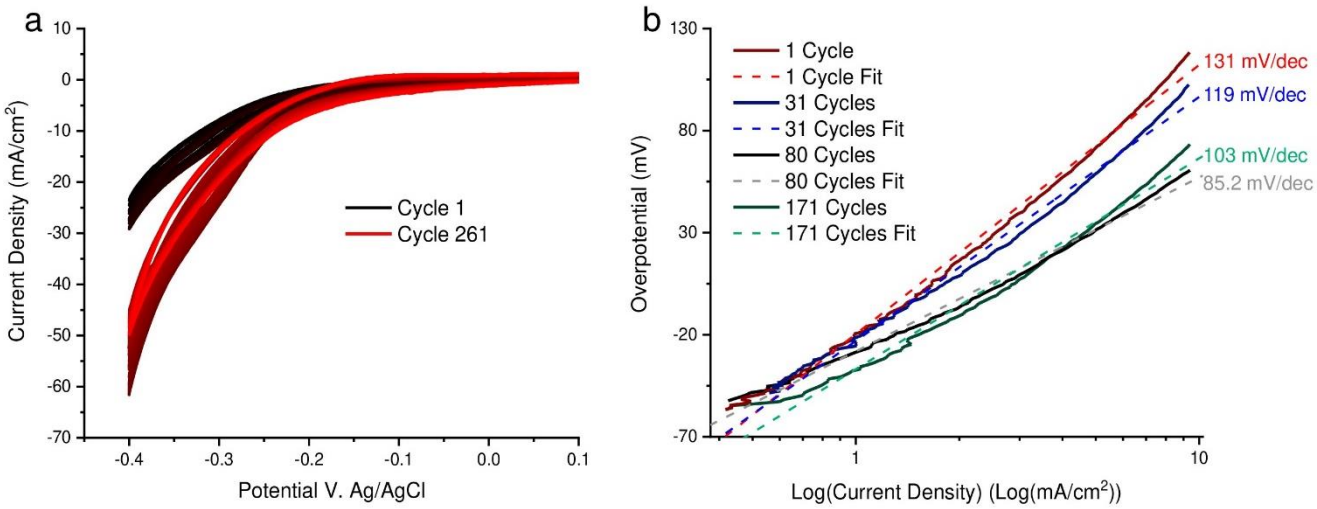

Figure 3.3. HER measurement of 1-L MoS_2 microelectrochemical reactor and analysis of catalytic performance. **a.** Cyclic voltammograms plotted every 9 cycles of the HER reaction using monolayer MoS_2 as the working electrode. 0.5 M H_2SO_4 was used as the electrolyte. 264 cyclic voltammograms was measured using a voltage window of 0.2 to -0.4 V vs Ag/AgCl with saturated KCl with a sweep rate of 5 mV/s. The line color transitions from black to red with increasing cycle number. **b.** Tafel plot of cyclic voltammetry cycles 1, 31, 80, and 171. The experimental data is plotted with solid lines, while the dotted lines show the result of the linear fit used to extract the Tafel slope noted on the right side of the figure.

The Tafel slope can give insight into the potential mechanism of the observed change in catalytic activity. The hydrogen evolution reaction is known to occur via three elementary reactions[26]:

$$H_2O + e^- \rightleftharpoons H(a) + OH^- \quad \text{(Volmer)} \tag{1}$$

$$H_2O + H(a) + e^- \rightleftharpoons H_2(g) \quad \text{(Heyrovsky)} \tag{2}$$

$$2H(a) + e^- \rightleftharpoons H_2(g) \quad \text{(Tafel)} \tag{3}$$

HER always begins with the Volmer step but can then proceed either through the Heyrovsky or Tafel step. For 1-L MoS_2, the 2nd step is usually the Heyrovsky reaction[27]. Each of these reactions will result in a unique Tafel slope when they are the rate determining step (RDS) of the reaction. These slopes are 120 mV/dec, 40 mV/dec, and 30 mV/dec for the Volmer, Heyrovsky, and Tafel steps, respectively[28]. Based on this knowledge, the RDS for this 1-L MoS_2 device is the Volmer step, as the Tafel slope for the first HER cycle was measured to be 131 mV/dec, close to the theoretical value of 120 mV/dec. However, by 80 cycles, the Tafel slope decreases to 85.2 mV/dec. This indicates a change in the RDS to the Heyrovsky reaction, indicating the HER proceeds through the Volmer-Heyrovsky mechanism. While the measured value of 85.2 mV/dec is larger than the theoretical value for Heyrovsky reaction, this higher-than-expected value for the Tafel slope is documented in other reports[15]. In this case, it may be due to the accumulation of H_2 at the electrocatalyst surface, or because of large contact resistance between the MoS_2 flake and metal contacts. An alternative explanation could be that the enhancement of the catalytic current may instead be the result of defect-enhanced conductivity, or lowered contact resistance by a defect-induced 1H to 1T phase transition[41]. However, the contacts, as well as the conductive pathway from the contact to the exposed area of the flake is insulated by the PMMA layer, preventing the formation of defects in this region and negating these explanations. Therefore, the enhanced catalytic activity must be caused by some modification of the 1-L MoS_2 that reduces the free energy of the adsorbed hydrogen intermediate. Tsai et al. performed theoretical calculations that show increasing the sulfur vacancy concentration in 1-L MoS_2 results in a decrease in the free energy of hydrogen absorbed on the surface[15]. The reduction in energy of this state would cause a shift to a Heyrovsky RDS, resulting in enhanced kinetics and a decreased Tafel slope. The authors also demonstrate that the application of a sufficiently reducing potential to monolayer MoS_2 in acidic

electrolyte induces the formation of sulfur vacancies as the sulfur reacts to form H_2S[15]. Thus, the observed increase in catalytic activity must be due to the formation of sulfur vacancies during catalytic cycling.

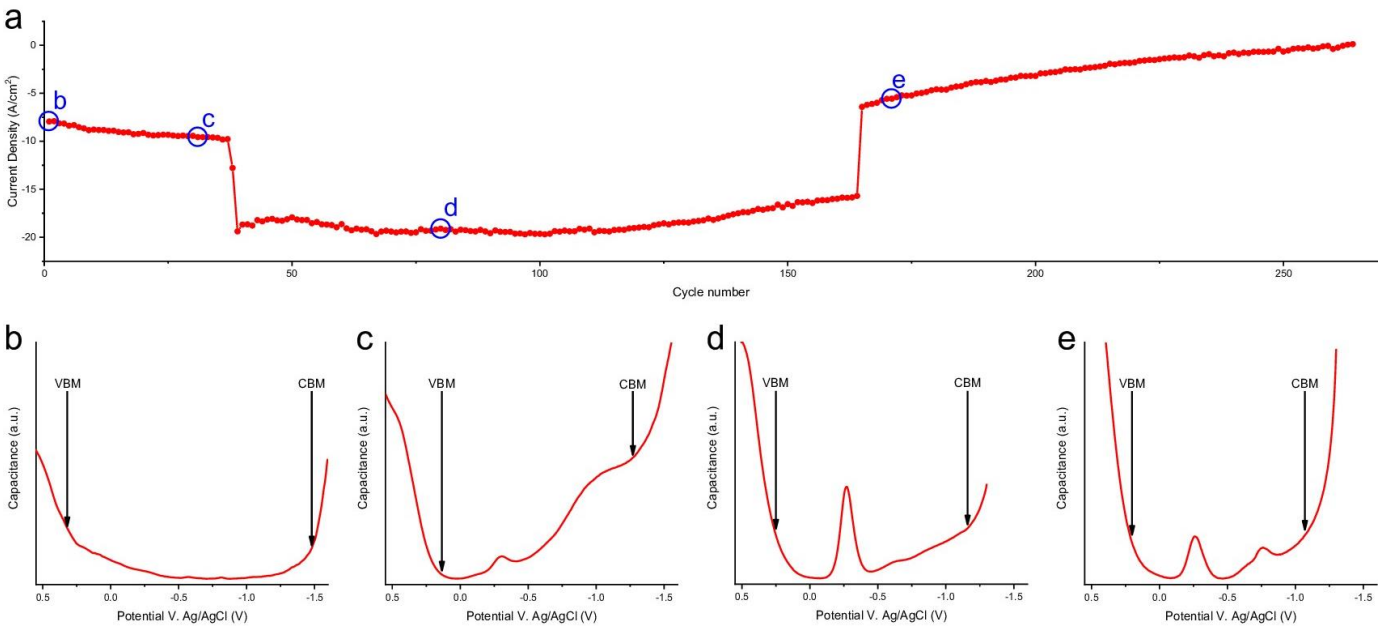

Figure 3.4. EQCS measurement of 1-L MoS_2 during HER catalytic cycling. **a.** The current density of the 1-L MoS_2 device at -0.3 V V. Ag/AgCl during catalytic cycling (0.5 M sulfuric acid electrolyte). The blue circles indicate the cycle immediately after the EQCS measurements shown in **b**-**e**. This value of the potential is just after the -0.197 V formal reduction potential of hydrogen. This value was chosen to avoid any instability in the current due to changes in the sample or bubble formation. **b-e**. EQCS results measured using the ionic liquid 1-butyl-3-methylimidazolim tetrafluoroborate ([BMIM][BF_4]) as the electrolyte. The spectra are normalized to a common peak at 0.68 V (Supplementary figure 3.S4-7). For these measurements, the reference electrode is changed to a Ag/AgCl wire immersed in a 0.1 M solution of BMIM chloride in [BMIM][BF_4]. The spectra in **b**-**e** are measured prior to the 1st, 31st, 81st, and 171st cycles and the extracted values of the bandgaps are 1.8 eV, 1.42 eV, 1.41 eV, and 1.27 eV, respectively.

The EQCS technique is employed to investigate the hypothesis that the observed change in catalytic activity is due to the formation of sulfur vacancies, which modify the electronic structure of 1-L MoS_2. Our previous work has shown that the EQCS technique can be used to measure the DOS and electronic structure of materials in ambient conditions, as the quantum capacitance is directly proportional to the DOS (chapter 2). To clearly visualize the trend in the catalytic current, the current density is plotted as a function of cycle number in Figure 3.4a. To assess the evolution of the electronic structure during cycle, EQCS is performed before the 1^{st}, 31^{st}, 81^{st}, and 171^{st} HER cycles. Looking at the current density in Figure 3.4a, these correspond to points in the cycling where: (i) the MoS_2 is pristine and shows low current density (Figure 3.4a point b); (ii) after some increase in the catalytic current and just before a rapid enhancement of the catalytic performance (Figure 3.4a point c); (iii) after the catalytic current reaches its maximum value (Figure 3.4a point d); (iv) and after the catalytic current experiences a major decline (Figure 3.4a point e). The initial EQCS spectrum shows a bandgap free of peaks with a value of 1.8 eV, indicating pristine 1-L MoS_2 (Figure 3.4b)[29]. After 30 cycles, the EQCS spectrum shows a decrease in bandgap to 1.42 eV, and the appearance of a peak around -0.3 V V. Ag/AgCl. Comparing to STS results, this peak can be attributed to undersaturated molybdenum d-orbitals resulting from individual sulfur vacancies formed during cycling. As stated prior, these defects are known to increase HER performance[30]. The decrease in the bandgap can also be explained by the presence of these vacancies, which reduce the splitting of the Mo d-orbitals that form the band edges[31,42]. STS has also been used to observe the decrease in the 1-L MoS_2 bandgap in the presence of sulfur vacancies[43]. At 80 cycles, the increasing concentration of sulfur vacancies causes the bandgap to decrease further to 1.41 eV, and the peak at -0.3 V V. Ag/AgCl to increase in height. This electronic structure should be the most favorable for HER, as it exhibits the lowest Tafel slope. The large

intensity of the sulfur vacancy peak is likely responsible for this ideal behavior, since the energy of absorbed hydrogen is stabilized by the overlap of the hydrogen s-orbital with the undersaturated molybdenum d-orbitals[32]. Finally, after 170 cycles, the bandgap decreases once more to 1.27 eV. The intensity of the sulfur vacancy peak decreases as a new peak appears within the conduction band. The decrease in the number of states around -0.3 V V. Ag/AgCl could explain the decline in catalytic activity, as the energy of the absorbed protons would become less favorable due to this change in electron density. Tsai et al. demonstrated that with increasing sulfur vacancy concentration, the energetics favor additional vacancies forming next to preexisting vacancies to form clusters[15]. This would result in a reduction of the favorable single sulfur vacancies, resulting in a lower DOS. This explanation is also supported by the appearance of a new peak at -0.76 V V. Ag/AgCl in the conduction band, where vacancy clusters such as V_{MoS6} are predicted to enhance electron density[19].

To further support the modulated catalytic activity being the result of the formation of vacancies, conductive atomic force microscopy (cAFM) is performed to image the vacancies formed in the MoS_2 lattice at the previously selected points during HER cycling. To maximize the possibility of successfully obtaining atomic resolution images of defects, 4 samples were prepared using the gold-assisted exfoliation method[33]. The method results in many few layer flakes with a large area on a gold coated wafer chip, enabling the facile establishment of a conductive connection between the cAFM stage potential bias and the MoS_2 few-layer flakes. A drawback of this method is that very thin flakes (1-3 layers) tend to have pinholes due to uneven interaction with the relatively rough surface of the gold. To avoid these holes, cAFM measurements were performed on 5-layer thick flakes. Though thicker than the flakes used for the previous measurements, it is reasonable to assume the 5-layer thick flake is a good proxy for the monolayer as the vacancy formation

energy should be nearly identical. Even comparing a monolayer to a bulk flake, the difference in the sulfur vacancy formation energy is only 0.1 eV[34]. One sample was left in its pristine state, while the other samples were subjected to HER cycling for 30, 80, and 170 cycles under identical conditions to those previously described. It should be noted that although each image was captured at the same sample-tip bias, the contrast can alternate so that atoms either appear bright on a dark background, or dark on a bright background. This effect is documented in the literature, and likely is a result of varying interaction between the MoS_2 flake and the substrate in different positions on the sample[35].

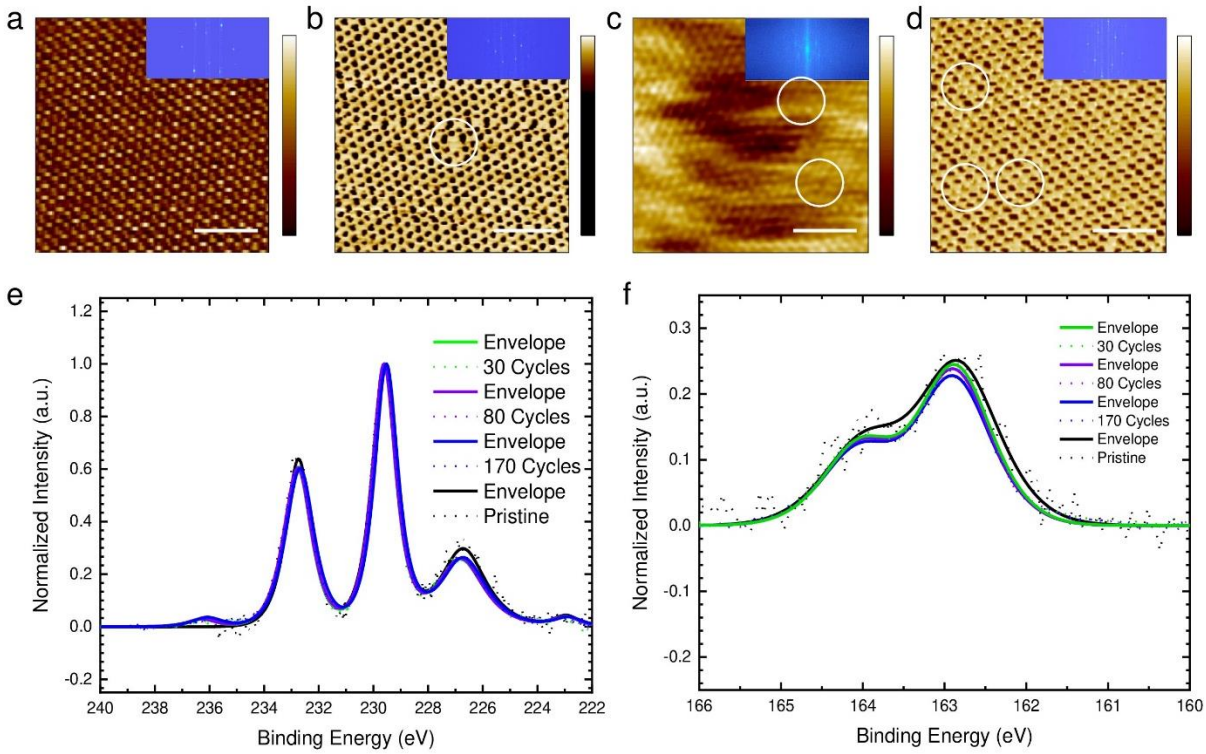

Figure 3.5. Imaging and quantification of vacancies in 5-L MoS_2. a. Atomic resolution cAFM images of 5-L MoS_2 in pristine condition, **b.** after 30 HER cycles, **c.** after 80 HER cycles, **d.** and after 170 HER cycles. Images were captured with a sample bias of -0.4 V. Scale bar: 2 nm. Current

range (gradient): 275 pA, 10 nA, 16 nA, and 120 nA, respectively. White circles are used to indicate sulfur vacancies. The 2d FFT image is shown in the inset. **e.** Overlayed XPS spectra showing the molybdenum 3d and **f.** sulfur 2p peak for 5-L MoS_2 in pristine condition, after 30, 80, and 170 HER cycles. The solid lines show the parametric fit, while the dotted lines show the experimental spectrum.

Figure 3.5a shows the atomic resolution cAFM image of the pristine 5-L MoS_2 flake. Notably, no dark spots, corresponding to sulfur vacancies, can be observed in the image. After 30 cycles, missing atoms (highlighted with white circles) become visible in the image (Figure 3.5b). These can be assigned as sulfur vacancies due to their very localized effect on the conductivity of the MoS_2[35]. The number of spots increases after 80 cycles (Figure 3.5c). These images clearly support the explanation of enhanced catalytic activity by formation of sulfur vacancies by providing visual proof of the appearance of vacancies with cycling. Interestingly, at 170 cycles, not only are there more single vacancies, but also missing atoms can be seen in close proximity, which suggests the formation of line vacancies (Figure 3.5d). This observation aligns well with the fact that the calculated total energy of sulfur vacancies is lowered in a clustered configuration compared to dispersed vacancies[31]. This is clear evidence demonstrating that the eventual decline in the HER performance with cycling is due to the conversion of individual sulfur vacancies to clusters[15].

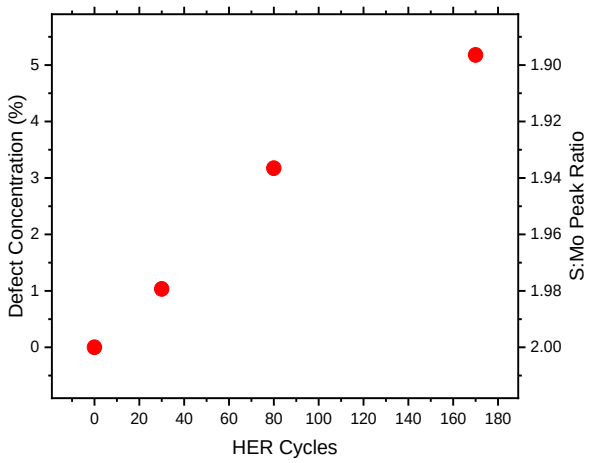

Figure 3.6. Sulfur vacancy concentration in the 1-L MoS_2 electrocatalyst. Vacancy concentrations (left axis) are calculated for the pristine flake, after 30 cycles, after 80 cycles, and after 170 cycles. The vacancy concentrations are 0, 1.04, 3.17, and 5.18 %. The vacancy concentrations are calculated from the ratio of the S to Mo peak area (right axis).

Though the cAFM images confirm the presence of sulfur vacancies, the difficulty in obtaining such images limits the ability to capture enough images to obtain a statistically relevant estimation of the number of vacancies. Fortunately, it has been demonstrated that comparing the ratio of the S 2p and Mo 3d peak area measured by XPS is a practical method to estimate sulfur vacancy concentrations[15]. Inspired by this, XPS spectra are captured for each of the devices imaged using cAFM. From Figure 3.5 e-h, it is apparent that the S:Mo peak ratio decreases with cycle number. This ratio is then used to extract an approximate defect concentration at different cycle numbers (Figure 3.6). The vacancy concentration extracted from the XPS shows an increase with cycle number, thereby confirming the change in the electrocatalytic performance of 1-L MoS_2 with time is indeed due to the formation of these vacancies. The ideal HER performance is observed at a sulfur vacancy concentration of 3.17 %. Additionally, it is likely that defect clusters only become

common after a vacancy concentration of 3.17 % is reached, as these clusters were only observed by cAFM in the device with 5.18 % vacancies.

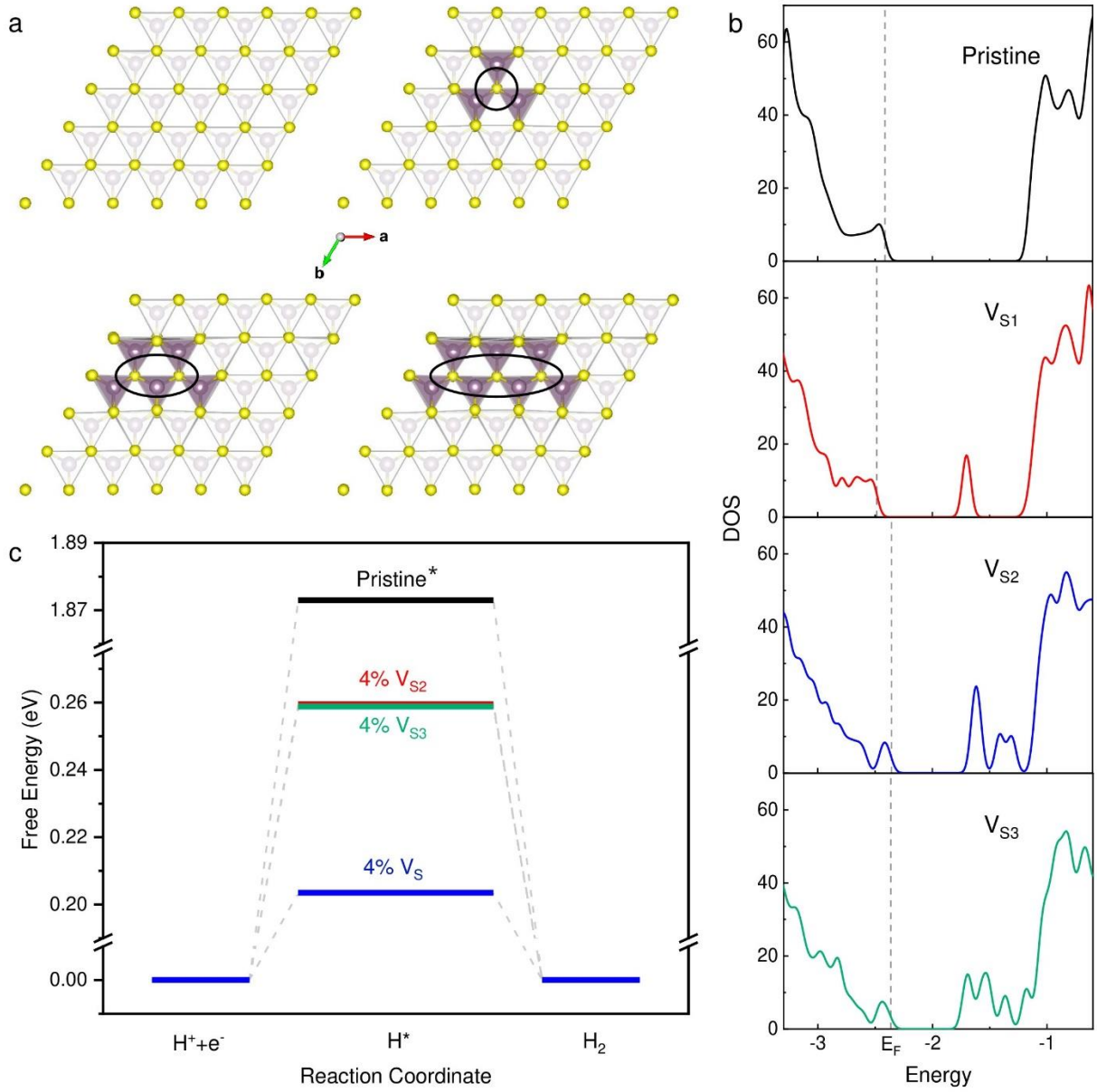

Figure 3.7. Simulated density of states reaction coordinate diagram. a. 5x5 unit cells used in the simulations. The location of sulfur vacancies on the top layer are circled in black. Sulfur atoms are shown in yellow, the unexposed molybdenum in faint purple, and the exposed molybdenum near the vacancies in dark purple. The coordination region around the exposed molybdenum is

shaded in purple. Clockwise from the top left, the structures show the pristine MoS_2, MoS_2 with a mono-sulfur vacancy, MoS_2 with a di-sulfur vacancy, and MoS_2 with a tri-sulfur vacancy. **b.** Simulated density of states for each of the structures in **a**. The vertical dotted line in each panel indicated the position of the Fermi energy at 0 K. **c.** Calculated reaction coordinate diagram showing the free energy of the absorbed hydrogen intermediate for each of the structures in **a**. The free energy of the reactants and products are assumed to be equal and taken as the zero reference point. *The value for the intermediate free energy on pristine MoS_2 is taken from ref. 40.

As mentioned prior, the proposed mechanism for the enhancement, then decline in the catalytic performance of 1-L MoS_2 is the inducement of a favorable electronic structure by isolated sulfur vacancies, then unfavorable structure by vacancy clusters. The EQCS results provide excellent experimental support for this explanation. However, to complete this argument, computational results are necessary to vet the claims made based on the experimental evidence. Using the crystal structures observed by cAFM, the density of states and hydrogen adsorption energies are calculated. Figure 3.7a shows the relaxed geometry of 5x5 unit cells representing pristine MoS_2 and the three defect structures observed by cAFM. Each defect structure corresponds to 4% of the defect type, or a total sulfur vacancy concentration of 4% (V_{S1}), 8% (V_{S2}), and 12% (V_{S3}). DFT is applied to simulate the DOS of states for each cell, assuming periodic boundary conditions (Figure 3.7b). As observed in EQCS spectra, the bandgap decreases with the increasing number of missing sulfur atoms. Additionally, like the effect seen in the experimental spectrum in figure 3.4c, the presence of mono-sulfur vacancies introduces a single peak in the bandgap of the computational DOS (figure 3.4b). As stated previously, this peak at -1.7 eV overlaps with the energy of the hydrogen s-orbital, thereby reducing the free energy of the absorbed hydrogen intermediate[32]. By contrast, the di- and tri-sulfur vacancies introduce peaks that cause a downshift

of the conduction band minimum, and both contribute fewer states at -1.7 eV. The consequence of this can been seen in figure 3.7c, which shows that while all the defect types lower the free energy of the absorbed hydrogen intermediate, the mono-sulfur vacancy, which produces a density of states with the highest overlap with the hydrogen s-orbital, results in the smallest free energy of the reaction intermediate. Thus, as observed in the cyclic voltammetry and Tafel slopes, this defect type will provide the greatest enhancement of catalytic activity. Once these mono-sulfur vacancies are converted into clusters, the free energy of the absorbed hydrogen intermediate will increase, and catalytic activity will decline.

3.5 Conclusion

In this paper, the behavior of 1-L MoS_2 as an HER catalyst over time was measured. The catalytic activity of the material was observed to increase, and then decrease over the course of the experiment. This behavior was attributed to the electrochemical generation of sulfur vacancies, which at lower concentrations exist as favorable point defects, but with time and increasing concentration grow to unfavorable clusters. The presence of the vacancies was confirmed by conductive AFM imaging and XPS. When the vacancies are present as point defects, they cause a peak in the DOS contributed by unsaturated molybdenum d-orbitals to form in the bandgap. This peak overlaps with the hydrogen s-orbital and results in decreased hydrogen adsorption energy, thereby reducing the barrier to hydrogen absorption, which is the RDS of HER on monolayer MoS_2. This results in an increase in catalytic performance, which is further enhanced by the formation of additional point defects. However, past a certain concentration threshold, the vacancies will grow into clusters, which are unfavorable for HER, and the catalytic activity is reduced. This is supported by the EQCS spectra and computational results.

To our knowledge, this is the first time this is the first time the ideal native defect concentration and structure for 1-L MoS_2 as an HER electrocatalyst has been identified experimentally. Experiments also identified the mechanism of failure of this material. This is missing in the literature, as most studies of this system focus on the initial performance of this material. These results show that varying the concentration of defects in MoS_2 is a controllable method to tune the electronic structure of the material, both for bulk properties (bandgap) and in-gap states, and that the catalytic performance is greatly influenced by defects[36]. However, the evidence provided here also indicates that defects can be detrimental to material performance, meaning care must be taken when using defects as a means of functionalizing a material. These results have broad applications, from creating in-gap states for catalysis or sensing, to controlling band alignment for P-N junctions[37,38]. By combining functional property measurements, in-situ measurements of electronic structure, crystal structure characterization, and computation, we were to clearly describe the structure-property relationships of this material. Eventually, such a strategy can be used to uncover design rules for synthesizing materials with desired properties, enabling a transition from trial and error to rational design of functional materials[39].

3.6 References

1 Geim, A. K. Graphene: Status and prospects. *Science* **324,** 1530–1534 (2009).

2 Susarla, S. *et al.* Quaternary 2d transition metal Dichalcogenides (TMDS) with tunable bandgap. *Advanced Materials* **29,** (2017).

3 Allain, A., Kang, J., Banerjee, K. & Kis, A. Electrical contacts to two-dimensional semiconductors. *Nature Materials* **14,** 1195–1205 (2015).

4 Hu, Z. *et al.* Two-dimensional transition metal dichalcogenides: Interface and defect engineering. *Chemical Society Reviews* **47,** 3100–3128 (2018).

5 Mak, K. F., He, K., Shan, J. & Heinz, T. F. Control of Valley polarization in monolayer MoS_2 by Optical Helicity. *Nature Nanotechnology* **7,** 494–498 (2012).

6 Radisavljevic, B., Radenovic, A., Brivio, J., Giacometti, V. & Kis, A. Single-layer MOS2 transistors. *Nature Nanotechnology* **6,** 147–150 (2011).

7 Novoselov, K. S. *et al.* Two-dimensional atomic crystals. *Proceedings of the National Academy of Sciences of the United States of America* **102**, 10451–10453 (2005).
8 Cao, Y. *et al.* Correlated insulator behavior at half-filling in magic-angle graphene superlattices. *Nature* **556,** 80–84 (2018).
9 Tyagi, D. *et al.* Recent advances in two-dimensional-material-based sensing technology toward health and Environmental Monitoring Applications. *Nanoscale* **12,** 3535–3559 (2020).
10 Hinnemann, B. *et al.* Biomimetic Hydrogen Evolution: MoS_2 nanoparticles as catalyst for hydrogen evolution. *Journal of the American Chemical Society* **127,** 5308–5309 (2005).
11 Chen, J. *et al.* Mechanism of highly enhanced hydrogen storage by two-dimensional 1T′ MoS_2. *Physical Chemistry Chemical Physics/PCCP*. *Physical Chemistry Chemical Physics* **22**, 430–436.
12 Sun, Y. *et al.* First-principles study of the catalytic properties of Co-doped molybdenum disulfide nanoribbons for the hydrogen evolution reaction. *Journal of Applied Physics* **128**, (2020).
13 Zhang, M., Guo, Z., Gellman, A. J., Salvador, P. A. & Rohrer, G. S. Influence of the molten SrCl2 treatment on the surface structure and photochemical reactivities of $SrTiO_3$. Applied Surface Science 638, 158111 (2023).
14 Vancsó, P. *et al.* The intrinsic defect structure of exfoliated MoS_2 single layers revealed by Scanning Tunneling Microscopy. *Scientific Reports* **6**, (2016).
15 Tsai, C. *et al.* Electrochemical generation of sulfur vacancies in the basal plane of MoS_2 for hydrogen evolution. *Nature Communications* **8**, (2017).
16 Man, P. *et al.* Salt-Induced High-Density Vacancy-Rich 2D MoS_2 for efficient hydrogen evolution. *Advanced Materials* **36**, (2023).
17 Ye, G. *et al.* Defects Engineered monolayer MoS_2 for improved hydrogen evolution reaction. *Nano Letters* **16**, 1097–1103 (2016).
18 Li, H. *et al.* Kinetic Study of Hydrogen Evolution Reaction over Strained MoS_2 with Sulfur Vacancies Using Scanning Electrochemical Microscopy. *Journal of the American Chemical Society* **138**, 5123–5129 (2016).
19 Chen, Y. *et al.* Tuning Electronic Structure of Single Layer MoS_2 through Defect and Interface Engineering. *ACS Nano* **12**, 2569–2579 (2018).
20 Zhou, W., Dong, L., Tan, L. & Tang, Q. First-principles study of sulfur vacancy concentration effect on the electronic structures and hydrogen evolution reaction of MoS_2. *Nanotechnology* **32**, 145718 (2021).
21 Yang, X. & Li, B. Monolayer MoS_2 for nanoscale photonics. *Nanophotonics* **9**, 1557–1577 (2020).
22 Wang, W., Zeng, X., Guo, Z., Ding, J. & Chen, X. Growth mechanism of continuous monolayer MoS_2 prepared by chemical vapor deposition. *IOP Conference Series. Materials Science and Engineering* **562**, 012074 (2019).
23 Ching, S., Dudek, R. & Tabet, E. Cyclic Voltammetry with Ultramicroelectrodes. *Journal of Chemical Education* **71**, 602 (1994).
24 Chen, S. *et al.* Tip-Based cleaning and smoothing improves performance in monolayer MoS_2 devices. *ACS Omega* **6**, 4013–4021 (2021).
25 Song, S. H. *et al.* Bandgap widening of phase quilted, 2D MoS_2 by oxidative intercalation. *Advanced Materials* **27**, 3152–3158 (2015).

26 De Chialvo, M. R. G. & Chialvo, A. C. Hydrogen evolution reaction: Analysis of the Volmer-Heyrovsky-Tafel mechanism with a generalized adsorption model. *Journal of Electroanalytical Chemistry* **372**, 209–223 (1994).
27 Shi, J. *et al.* Controllable growth and transfer of monolayer MoS2 on Au foils and its potential application in hydrogen evolution reaction. *ACS Nano* **8**, 10196–10204 (2014).
28 Shinagawa, T., Garcia-Esparza, A. T. & Takanabe, K. Insight on Tafel slopes from a microkinetic analysis of aqueous electrocatalysis for energy conversion. *Scientific Reports* **5**, (2015).
29 Tang, Q. & Jiang, D.-E. Stabilization and Band-Gap tuning of the 1T-MoS_2 monolayer by covalent functionalization. *Chemistry of Materials* **27**, 3743–3748 (2015).
30 Li, H. *et al.* Activating and optimizing MoS_2 basal planes for hydrogen evolution through the formation of strained sulfur vacancies. *Nature Materials* **15**, 48–53 (2015).
31 Zhou, W., Dong, L., Tan, L. & Tang, Q. First-principles study of sulfur vacancy concentration effect on the electronic structures and hydrogen evolution reaction of MoS_2. *Nanotechnology* **32**, 145718 (2021).
32 Ling, F. *et al.* Optimizing edges and defects of supported MoS_2 catalysts for hydrogen evolution via an external electric field. *Physical Chemistry Chemical Physics/PCCP*. *Physical Chemistry Chemical Physics* **20**, 26083–26090 (2018).
33 Velický, M. *et al.* Mechanism of Gold-Assisted exfoliation of Centimeter-Sized Transition-Metal dichalcogenide monolayers. *ACS Nano* **12**, 10463–10472 (2018).
34 Komsa, H.-P. & Krasheninnikov, A. V. Native defects in bulk and monolayer MoS_2 from first principles. *Physical Review. B, Condensed Matter and Materials Physics* **91**, (2015).
35 Sumaiya, S. A., Liu, J. & Baykara, M. Z. True Atomic-Resolution Surface Imaging and Manipulation under Ambient Conditions via Conductive Atomic Force Microscopy. *ACS Nano* **16**, 20086–20093 (2022).
36 Yanase, T., Uehara, F., Naito, I., Nagahama, T. & Shimada, T. Healing Sulfur Vacancies in Monolayer MoS2 by High-Pressure Sulfur and Selenium Annealing: Implication for High-Performance Transistors. *ACS Applied Nano Materials* **3**, 10462–10469 (2020).
37 He, Z. *et al.* Defect engineering in Single-Layer MoS_2 using heavy ion irradiation. *ACS Applied Materials & Interfaces* **10**, 42524–42533 (2018).
38 Park, J. *et al.* Single-Gate Bandgap opening of bilayer graphene by dual molecular doping. *Advanced Materials* **24**, 407–411 (2011).
39 Zhao, C. *et al.* Rational design of layered oxide materials for sodium-ion batteries. *Science* **370**, 708–711 (2020).
40 Zhao, N., Wang, L., Zhang, Z. & Li, Y. Activating the MOS2 basal planes for electrocatalytic hydrogen evolution by 2H/1T′ structural interfaces. *ACS Applied Materials & Interfaces* **11**, 42014–42020 (2019).
41 Kappera, R. *et al.* Phase-engineered low-resistance contacts for ultrathin MoS_2 transistors. *Nature Materials* **13**, 1128–1134 (2014).
42 Gali, S. M., Pershin, A., Lherbier, A., Charlier, J.-C. & Beljonne, D. Electronic and transport properties in defective MOS2: Impact of sulfur vacancies. *Journal of Physical Chemistry. C./Journal of Physical Chemistry. C* **124**, 15076–15084 (2020).
43 Liu, M. *et al.* Temperature-Triggered sulfur vacancy evolution in monolayer MoS_2/Graphene heterostructures. *Small* **13**, (2017).
44 Kresse, G. & Furthmuller, J. Efficient iterative schemes for ab initio total-energy calculations using a plane-wave basis set. *Phys. Rev. B* **54**, 11169–11186 (1996).

45 Kresse, G. & Furthmuller, J. Efficiency of ab-initio total energy calculations for metals and semiconductors using a plane-wave basis set. *Comput. Mater. Sci.,* **6**, 15–50 (1996).
46 Kresse, G. & Joubert, D. From ultrasoft pseudopotentials to the projector augmented-wave method. *Phys. Rev. B* **59**, 1758–1775 (1999).
47 Perdew, J. P., Burke, K. & Ernzerhof, M. Generalized gradient approximation made simple. *Phys. Rev. Lett.* **77**, 3865–3868 (1996).
48 Grimme, S., Antony, J., Ehrlich, S. & Krieg, H. A consistent and accurate ab initio parametrization of density functional dispersion correction (DFT-D) for the 94 elements H-Pu. *J. Chem. Phys.* **132**, 154104 (2010).

3.7 Acknowledgments:

Funding: This research was funded by U.S. Department of Energy, Office of Science, Basic Energy Sciences, Division of Materials Sciences and Engineering, under Award KC020105-FWP12152 Pacific Northwest National Laboratory (PNNL) was operated by Battelle for the Department of Energy under contract no. DE-AC05-76RLO1830. J. H. acknowledges the support of University of Washington Molecular Engineering Materials Center (MEM·C) NSF grant DMR-1719797. This material is based in part upon work supported by the state of Washington through the University of Washington Clean Energy Institute. Part of this work was conducted at the Washington Nanofabrication Facility / Molecular Analysis Facility, a National Nanotechnology Coordinated Infrastructure (NNCI) site at the University of Washington with partial support from the National Science Foundation via awards NNCI-1542101 and NNCI-2025489.

3.8 Supplementary Information

3.8.1 Fitting of confocal Raman spectra

The Raman spectra are fit in the OriginLab software using a nonlinear least-squares approach. Two Gaussian peaks with a constant baseline are used. The xc value for the peaks is used to determine their separation.

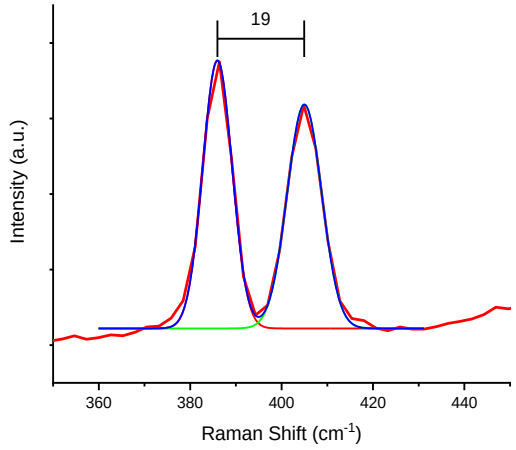

Figure 3.S1. Confocal Raman spectrum of 1-L MoS_2 fitted with Gaussian peaks.

Model	**Gauss**	
Equation	y=y0 + (A/(w*sqrt(pi/2)))*exp(-2*((x-xc)/w)^2)	
Plot	Peak1(Intensity)	Peak2(Intensity)
y0	360.33708 ± 8.5651	360.33708 ± 8.5651
xc	385.95437 ± 0.0563	404.9965 ± 0.07298
w	6.40524 ± 0.12003	7.52434 ± 0.15738
A	14240.72345 ± 259.53145	13973.97188 ± 288.7846
Reduced Chi-Sqr	1045.17	
R-Square (COD)	0.997345	

Adj. R-Square	0.996586

Table 3.S1. Parameters used to fit the spectrum shown in Figure S1

3.8.2 Fitting of confocal PL spectra

The PL spectra are fit in the OriginLab software using a nonlinear least-squares approach. A Lorentzian peak with a constant baseline is used. The xc value for the peaks is used to determine the PL emission energy.

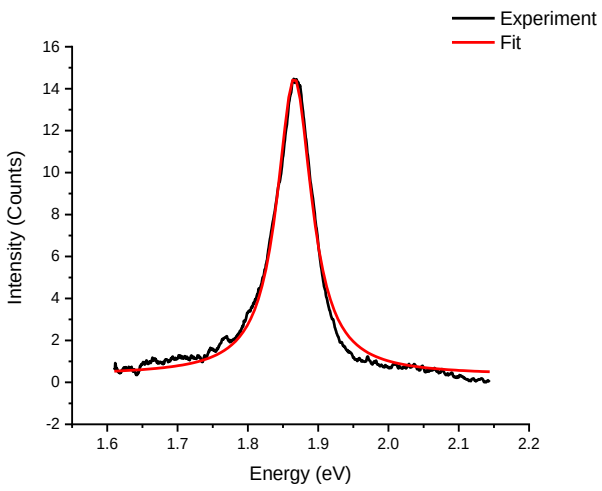

Figure 3.S2. Confocal PL spectrum of 1-L MoS_2 fitted with Lorentzian peak.

Model	**Lorentz**
Equation	y = y0 + (2*A/pi)*(w/(4*(x-xc)^2 + w^2))
Plot	Peak 1 Intensity
y0	0.34213 ± 0.01795
xc	1.86604 ± 1.25344E-4

w	0.05998 ± 4.29849E-4	
A	1.33487 ± 0.00809	
Reduced Chi-Sqr		0.136818
R-Square (COD)		0.988972
Adj. R-Square		0.988935

Table 3.S2. Parameters used to fit the spectrum shown in Figure S2

3.8.3 Extraction of the Tafel slope

The Tafel plot is generated by plotting the overpotential, calculated by taking the negative value of the formal potential of HER (-0.197 V. Ag/AgCl) subtracted from the applied voltage, against the $\log_{10}$ of the absolute value of the current. The region of the slope with low overpotential is selected to avoid coverage effects. The Tafel slope is then extracted by applying a linear fit using a least-squares method in the OriginLab software.

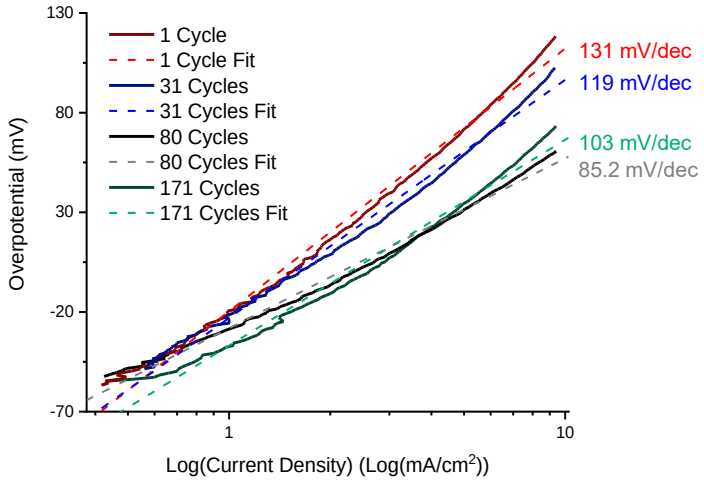

Figure 3.S3. Tafel analysis of four HER cycles with linear fits. The Tafel slope is noted next to the corresponding line.

Plot	1 Cycle
Equation	y = a + b*x
Weight	No Weighting
Intercept	0.17738 ± 4.82173E-4
Slope	0.13178 ± 8.89193E-4
Residual Sum of Squares	0.003568
Pearson's r	0.996062
R-Square (COD)	0.99214
Adj. R-Square	0.992095
Plot	31 Cycles
Equation	y = a + b*x
Weight	No Weighting
Intercept	0.17402 ± 4.92219E-4
Slope	0.11949 ± 8.86018E-4
Residual Sum of Squares	0.002393
Pearson's r	0.995902
R-Square (COD)	0.991821
Adj. R-Square	0.991766
Plot	81 Cycles
Equation	y = a + b*x
Weight	No Weighting
Intercept	0.1689 ± 3.99799E-4
Slope	0.08519 ± 7.40899E-4
Residual Sum of Squares	0.001037
Pearson's r	0.995791
R-Square (COD)	0.991599
Adj. R-Square	0.991524
Plot	171 cycles
Equation	y = a + b*x

Weight	No Weighting
Intercept	0.16017 ± 7.12933E-4
Slope	0.10326 ± 0.00126
Residual Sum of Squares	0.003504
Pearson's r	0.990598
R-Square (COD)	0.981285
Adj. R-Square	0.98114

Table 3.S3. Parameters used to fit the 4 Tafel curves shown in Figure S3.

3.8.4 Analysis of the electrochemical quantum capacitance spectroscopy results

The bandgap of monolayer MoS_2 is extracted by performing a linear fit using the least squares method on the linear regions of the band edges and the bandgap. The position of the band edge is determined by where the linear fit of that edge and the bandgap insect. Gaussian error propagation is used to find the error in the band edge position and bandgap.

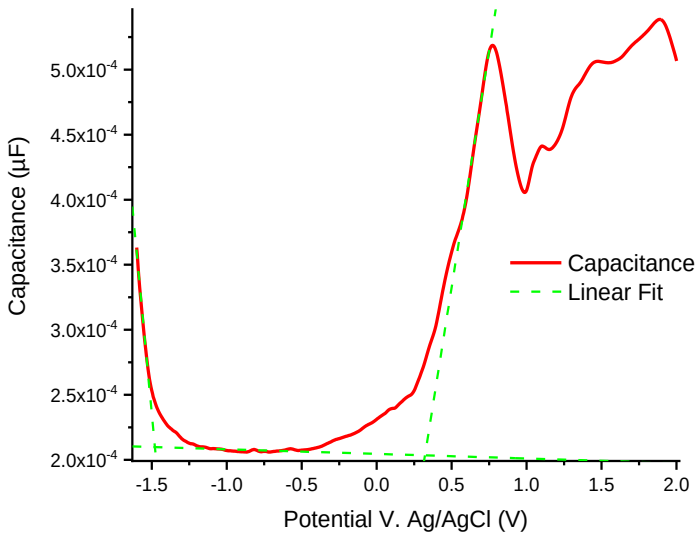

Figure 3.S4. EQCS spectrum of pristine 1-L MoS_2 with linear fits.

Linear Fit	CBM (line 1)	Bandgap	VBM (line 2)
Equation	$y_1 = m_1x_1 + b_1$	$y_1 = m_1x_1 + b_1$	$y_2 = m_2x_2 + b_2$
Intercept	-0.00161 ± 4.13-5	2.05E-4 ± 3.89E-7	-3.07E-5 ± 5.84E-6
Slope	-0.00123 ± 2.64E-5	-3.52E-6 ± 4.40E-7	7.27E-4 ± 9.12E-6
Residual Sum of Squares	8.30E-11	1.66E-10	2.76E-10
R-Square (COD)	0.99	0.31	0.99

VBM	CBM	Bandgap
0.32 ± 0.0090 V	-1.48 ± 0.046 V	1.8 ± 0.047 V

Table 3.S4. Parameters used to fit the linear regions of the pristine 1-L MoS_2 EQCS spectra and the extracted values of the valence band maximum, conduction band minimum, and the bandgap.

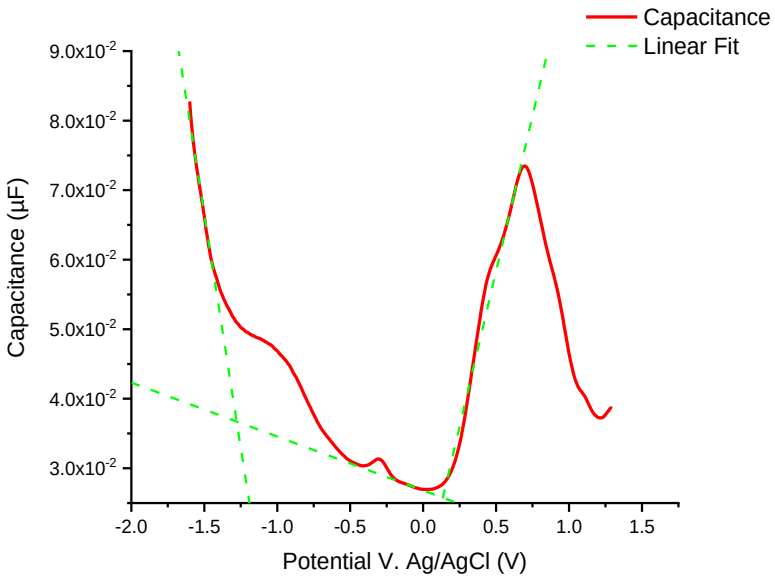

Figure 3.S5. EQCS spectrum of 1-L MoS_2 after 30 HER cycles with linear fits.

Linear Fit	CBM (line 1)	Bandgap	VBM (line 2)
Equation	$y_1 = m_1x_1 + b_1$	$y_1 = m_1x_1 + b_1$	$y_2 = m_2x_2 + b_2$
Intercept	-0.1348 ± 0.00299	0.0268 ± 6.79E-6	0.0137 ± 3.05E-4
Slope	-0.1342 ± 0.00198	-0.0078 ± 6.07E-5	0.0893 ± 5.014E-4
Residual Sum of Squares	1.02746E-5	3.77E-9	8.97E-9
R-Square (COD)	0.99	1.00	1.00

VBM	CBM	Bandgap
0.135 ± 0.003 V	-1.28 ± 0.031 V	1.42 ± 0.031 V

Table 3.S5. Parameters used to fit the linear regions of the EQCS spectra of 1-L MoS_2 after 30 HER cycles and the extracted values of the valence band maximum, conduction band minimum, and the bandgap.

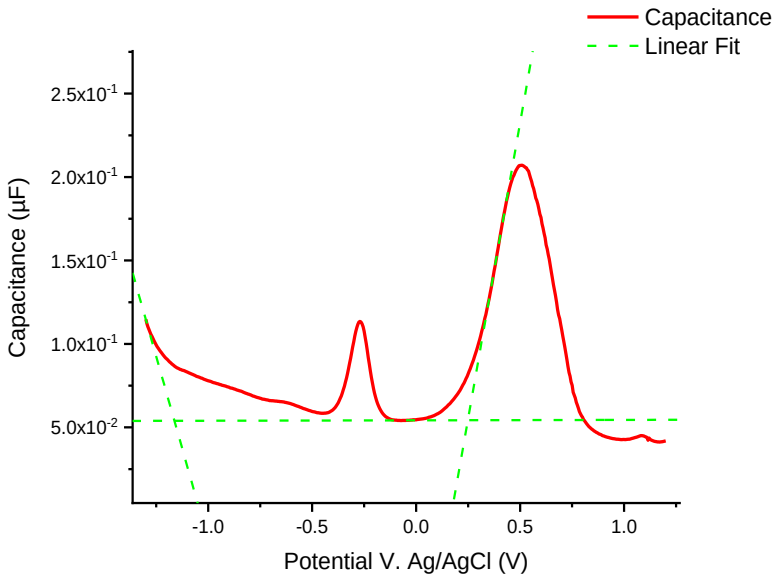

Figure 3.S6. EQCS spectrum of 1-L MoS_2 after 80 HER cycles with linear fits.

Linear Fit	CBM (line 1)	Bandgap	VBM (line 2)
Equation	$y_1 = m_1x_1 + b_1$	$y_1 = m_1x_1 + b_1$	$y_2 = m_2x_2 + b_2$
Intercept	-0.459 ± 0.052	0.054 ± 6.24E-5	-0.122 ± 0.00222
Slope	-0.441 ± 0.040	2.52E-4 ± 9.11E-4	0.709 ± 0.00586
Residual Sum of Squares	8.01645E-8	7.56E-8	2.34E-6
R-Square (COD)	0.98	0.00585	1.00

VBM	CBM	Bandgap
0.250 ± 0.0038 V	-1.16 ± 0.16 V	1.41 ± 0.16 V

Table 3.S6. Parameters used to fit the linear regions of the EQCS spectra of 1-L MoS_2 after 80 HER cycles and the extracted values of the valence band maximum, conduction band minimum, and the bandgap.

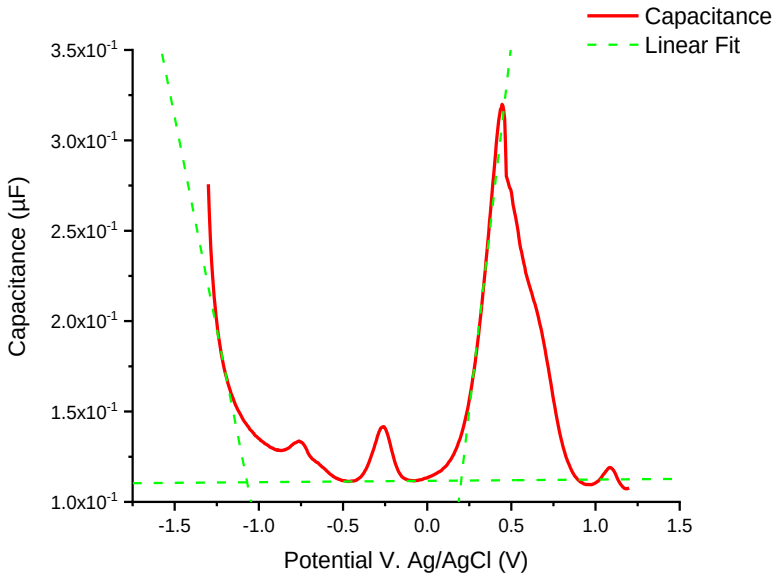

Figure 3.S7. EQCS spectrum of 1-L MoS_2 after 170 HER cycles with linear fits.

Linear Fit	CBM (line 1)	Bandgap	VBM (line 2)
Equation	$y_1 = m_1x_1 + b_1$	$y_1 = m_1x_1 + b_1$	$y_2 = m_2x_2 + b_2$
Intercept	-0.391 ± 0.0200	0.111 ± 8.92E-19	-0.05185 ± 0.00512
Slope	-0.469 ± 0.0161	7.28E-4 ± 9.41E-19	0.81105 ± 0.01654
Residual Sum of Squares	1.767E-5	7.79786E-31	1.72937E-4
R-Square (COD)	0.986	1	0.991

VBM	CBM	Bandgap
0.202 ± 0.008 V	-1.07 ± 0.055 V	1.27 ± 0.056 V

Table 3.S7. Parameters used to fit the linear regions of the EQCS spectra of 1-L MoS_2 after 170 HER cycles and the extracted values of the valence band maximum, conduction band minimum, and the bandgap.

3.8.5 Conductive AFM imaging

Conductive AFM images are collected at positive and negative sample-tip biases. As shown in Figure S8a and b, the bias only affects the contrast; that is, whether the atoms appear as bright or dark spots. As mentioned in the main text, this contrast also seems to be influenced by the monolayer flake's interaction with the substrate. The effect of the bias on the contrast is clearly demonstrated in Figure S8c, where the contrast switches from dark to light (the scan direction is bottom of image to top) when the bias is changed from -400 mV to 400 mV.

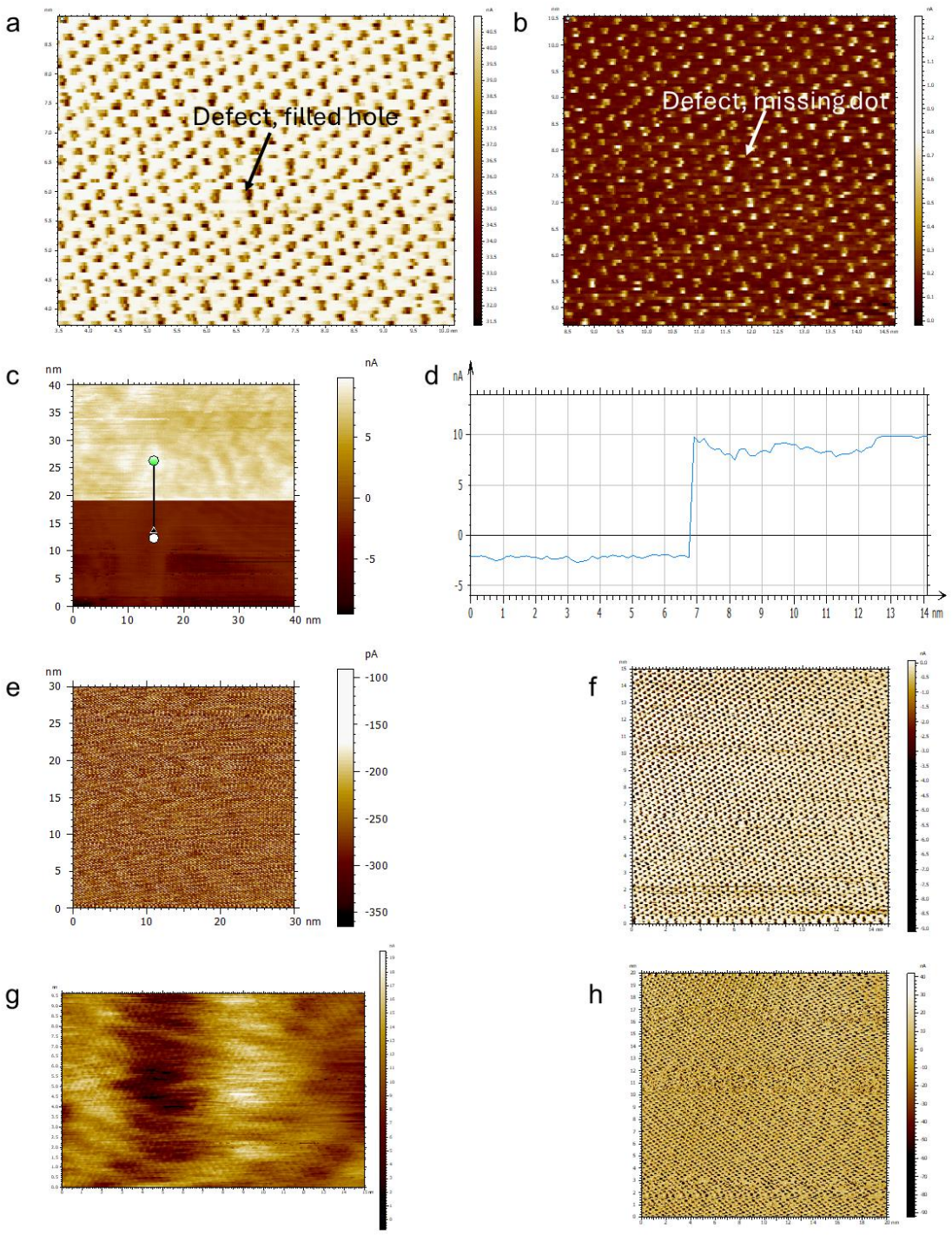

Figure 3.S8. Conductive AFM images and cross sections. a. Conductive AFM image of the device subjected to 30 HER cycles with a -400 mV bias and a **b.** positive 400 mV bias. Both images are taken in the same location. **c.** Conductive AFM image with the scan direction from bottom to top. The bias is changed from -400 mV to positive 400 mV at 19 nm on the y-axis. **d.** Current

profile along the cross-section shown in **c. e.** Full-sized image of pristine MoS_2, **f.** after 30 cycles, **g.** after 80 cycles, and **h.** after 170 cycles.

3.8.6 XPS Analysis

The unormalized XPS spectra are shown in Figure 3.S9. Notably, after catcalytic cycling, the S 2p peaks decrease (Figure 3.S9c). In addition to this, MoO_x peaks become vsible (Figure 3.S9c). This is likely due to the oxidation of some of the sulfur vacancies from exposure to air. Fortunately, this oxidation does not impede the calculation of vacancy concentration, as the oxide peak area can simply be included in the total Mo 3d peak area. The pristine spectra have a lower intensity owing to the fact that they were measured with 20 accumulations, while the rest were measured with 40 accumulations.

The peak ratios are extracted by from the XPS spectra by calculating the area under the S 2p and Mo 3d regions, dividing by the relevant sensitivity factor, and then taking the ratio of the results. In pristine MoS_2, this ratio should be 2. A normalization factor is found by dividing 2 by the measured ratio for the pristine device, which is applied to the other measured ratio. The difference between the pristine ratio and the normalized ratio for each device is calculated and divided by 2 to find the % sulfur vacancies present. These results are tabulated in Table 3.S9.

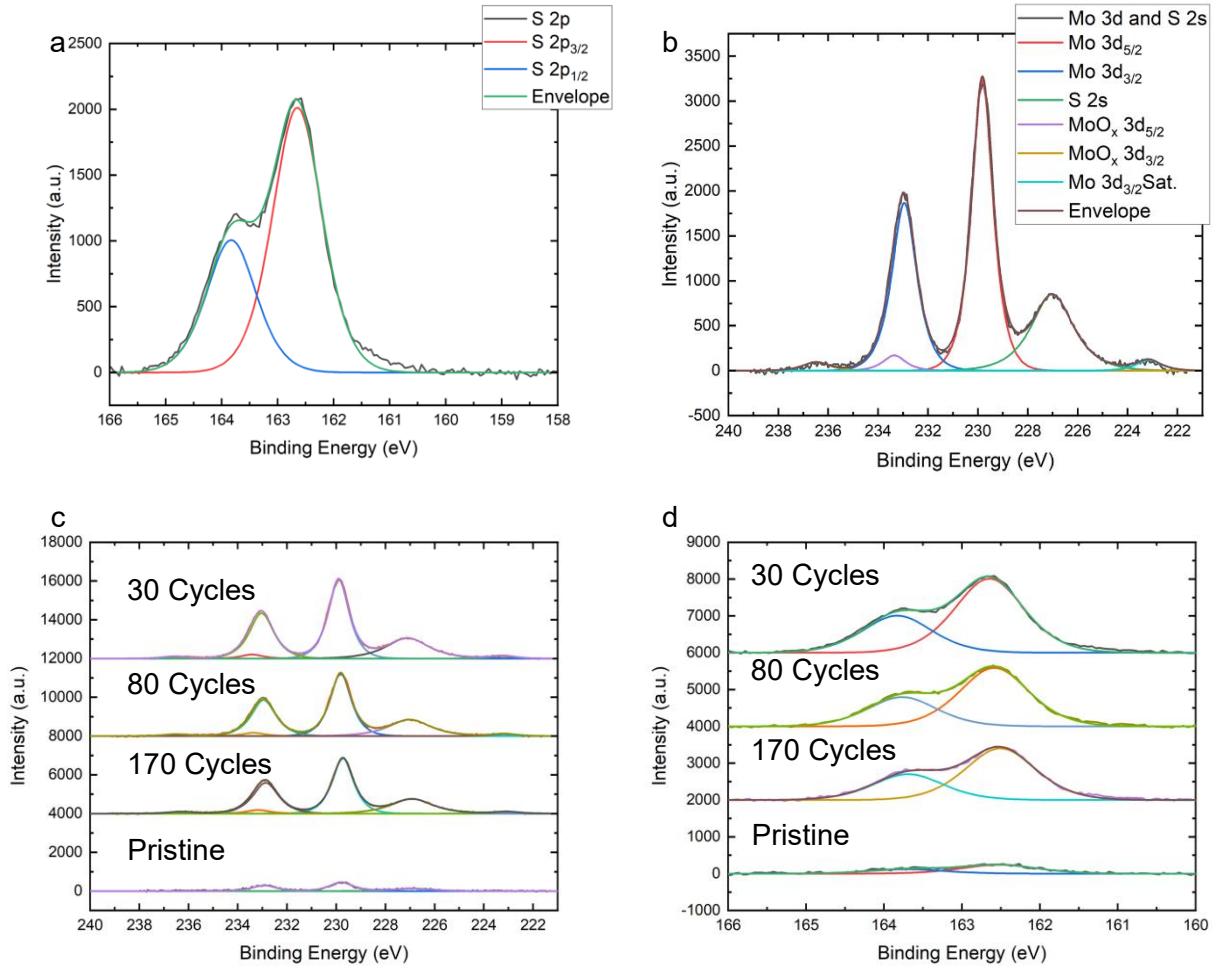

Figure 3.S9. XPS spectra of the cycled devices. a. XPS spectrum of the device cycled for 30 cycles for the S 2p and **b.** Mo 3d regions showing the peak assignments. **c.** Waterfall plot showing the spectra of each of the 4 devices in the Mo 3d region and the **d.** S 2P region.

	S:Mo ratio	Normalized to Bulk	Difference from Bulk	% Sulfur Vacancies
Bulk	2.191	2		0
170 Cycles	2.077	1.896	0.104	5.178
80 Cycles	2.121	1.937	0.063	3.172
30 Cycles	2.168	1.979	0.021	1.035

Table 3.S8 Peak ratios extracted from XPS and the calculated vacancy concentrations.

CURRICLUM VITAE

EDUCATION

University of Washington Expected 2024

PhD Candidate, Department of Chemistry

University of Washington class of 2018

BS in Chemistry with ACS certification

AWARDS

University of Washington Chemistry Undergraduate Research Award	June 2018
Clean Energy Institute Fellow	October 2020 - June 2021
Advanced Experience Program, Tech Due Diligence	October 2020 - June 2021
Clean Energy Institute Outreach Award	June 2021
Clean Energy Institute Education and Training Fellow	September 2021 – September 2022
ECS Pacific Northwest Section Student Award	October 2022

RELATED EXPERIENCE

Pacific Energy Network, Inc.

Electrical System Designer June 2016 – September 2018

Designed the chassis and electronics for a charger/inverter to use in PEN microgrid

Pacific Energy Network, Inc.

Engineering Researcher May 2015 – June 2016

Wrote reports on battery and fuel cell technologies for future projects

Pacific Energy Network, Inc.

Designer and Drafter July 2014 – May 2015

Drafted and designed substations and power plants

PUBLICATIONS AND PAPERS

Characterization of the Evolving Role of Defects in Determining the Electronic Structure and Electrochemical Behavior of Monolayer MoS_2. *In preparation for submission to JES*

Mitchell Kaiser, Hao Tang, Jose Ortiz-Garcia, Maria Sushko, Shuai Zhang, Ying Xia, Yuhuan Meng, Zbynek Novotny, Zdenek Dohnalek, Jun Liu.

Measuring and Manipulating Defect States in Two-Dimensional Materials with Electrochemical Capacitance. *Submitted to Nature Materials*

Mitchell Kaiser, Hao Tang, Jose Ortiz-Garcia, Maria Sushko, Shuai Zhang, Ying Xia, Yuhuan Meng, Zbynek Novotny, Zdenek Dohnalek, Jun Liu.

Epitaxial growth of 2D core-crown SnS_2-$SnSe_2$ heterostructure through interfacial modification with polyvinylpyrrolidone (PVP). *In preparation for submission to Angew. Chem. Int. ed.*

Lili L. Liu, Duo Song, Mitchell E. Kaiser, Jun Liu, James J. De Yoreo, Maria L. Sushko.

Control of Excited-State Proton-Coupled Electron Transfer by Ultrafast Pump-Push-Probe Spectroscopy in Heptazine-Phenol Complexes: Implications for Photochemical Water Oxidation. *The Journal of Physical Chemistry C*

Kathryn L. Corp, Emily J. Rabe, Xiang Huang, Johannes Ehrmaier, Mitchell E. Kaiser, Andrzej L. Sobolewski, Wolfgang Domcke, and Cody W. Schlenker

Structural Diversity in Cesium Bismuth Halide Nanocrystals. *Chemistry of Materials*

Sidney E. Creutz, Hongbin Liu, Mitchell E. Kaiser, Xiaosong Li, Daniel R. Gamelin

MEMBERSHIPS

American Chemical Association

Electrochemical Society, Pacific Northwest Section